Check for updates

Stochastic accretion of the Earth

Paolo A. Sossi [1✉], Ingo L. Stotz[2], Seth A. Jacobson [3], Alessandro Morbidelli[4] and Hugh St. C. O'Neill[5]

Chondritic meteorites are thought to be representative of the material that formed the Earth. However, the Earth is depleted in volatile elements in a manner unlike that observed in any chondrite, and yet these elements retain chondritic isotope ratios. Here we use *N*-body simulations to show that the Earth did not form only from chondrites, but by stochastic accretion of many precursor bodies whose variable compositions reflect the temperatures at which they formed. Earth's composition is reproduced when the initial temperatures of planetesimal- to embryo-sized bodies are set by disk accretion rates of $(1.08 \pm 0.17) \times 10^{-7}$ solar masses per year, although they may be perturbed by ^{26}Al heating on bodies formed at different times. Our model implies that a heliocentric gradient in composition was present in the protoplanetary disk and that planetesimals formed rapidly within ~1 Myr, consistent with radiometric volatile depletion ages of the Earth.

The terrestrial planets of our Solar System, including the Earth, are thought to represent the sum of progressive collisional growth of smaller bodies, whose size distribution evolved through time and space. In the classical model, collisions involve mostly nearby objects and lead to the formation of tens of Moon- to Mars-sized embryos within the lifetime of the protoplanetary disk (a few million years)[1]. Only after the disappearance of gas from the disk, which causes embryos to become dynamically unstable, is mixing between objects from different heliocentric distances expected over 10^7–10^8 yr timescales[2,3]. However, recent models suggest that the accretion of most of the Earth's mass occurred within the lifetime of the disk via the capture of sunward-drifting centimetre-sized 'pebbles' that initially formed at the 'snow line'[4,5].

Such models of the Earth's accretion may be tested by examining the chemical and isotopic composition of the bulk silicate Earth (BSE), which has been estimated from geological evidence[6]. The BSE is the Earth excluding its metallic core, which is inaccessible to detailed chemical scrutiny. In the BSE, refractory lithophile elements (RLEs) (refractory refers to an element that is calculated to condense from the solar nebula at a higher temperature than the main planet-forming elements, Mg, Si and Fe, and lithophile indicates that they do not enter the Earth's metallic core) occur in solar proportions relative to one another, whereas the abundances of moderately volatile lithophile elements decrease according to their calculated 50% nebular condensation temperatures (T_c^{50}) (Fig. 1). These elements have $T_c^{50} < 1{,}300$ K and include K, Rb, Zn and Cl, whose isotopic constitutions are similar to those measured in chondrites[7–10]. This observation precludes their depletion being the result of partial evaporative loss from the Earth or its precursors, which would have caused detectable isotopic fractionation[11,12].

Instead of partial evaporation, element depletion could occur without isotopic fractionation should the Earth have accreted from mixtures of components in which an element is either present in solar abundances relative to RLEs (and therefore with chondritic isotope ratios) or almost entirely absent, with the likelihood of its presence/absence being a function of its condensation temperature. As most elements are calculated to condense from the solar nebula gas over a narrow temperature window (a few tens of kelvin), the

condensation of one element should be nearly complete before that of the next element has begun[12,13]. If condensation ceases at some threshold temperature, T_0, a step-function pattern in the planetary body is produced when the CI- (Ivuna-type carbonaceous chondrites), Al-normalized abundance of element i, f_i, is plotted against T_c^{50} (ref. [14]). Since such step-like depletion patterns are observed in small, rocky bodies (for example, Vesta; Fig. 1), this feature was probably commonplace in the pebble- and planetesimal-sized building blocks of the Earth. The Earth instead exhibits a smoother decline in elemental abundance over a wider range of T_c^{50} (Fig. 1) that differs from any chondrite. Indeed, no mixture of the extant suite of chondritic meteorites can simultaneously reproduce the isotopic and chemical composition of the Earth[15,16].

Abundances (x) of element i normalized to CI and Al in both the Earth and Vesta increase with increasing T_c^{50} in a manner approximated by a cumulative normal distribution:

$$f_i^{\mathrm{CI,Al}} = \frac{(x_i/x_{\mathrm{Al}})_{\mathrm{body}}}{(x_i/x_{\mathrm{Al}})_{\mathrm{CI}}} = \frac{1}{2}\left[1 + \mathrm{erf}\left(\frac{T_c^{50} - T_0}{\sigma\sqrt{2}}\right)\right] \qquad (1)$$

The inflection point reflects the mean temperature, T_0, of the distribution, for which weighted fits yield $1{,}144 \pm 12$ K and $1{,}081 \pm 29$ K (1σ) for Earth and Vesta, respectively. The steepness of the sigmoid is described by σ, the standard deviation, approximating a step function at low σ (57 ± 17 K for Vesta) or a gradual curve at high σ (226 ± 16 K for Earth), both 1σ.

The mean temperatures experienced by the building blocks of the Earth (1 au) exceeded those of Vesta (2.36 au), consistent with, but not indicative of, a heliocentric gradient in composition. Any such gradient among precursor bodies set by the disk may have been subsequently perturbed by the ^{26}Al heating they experienced and/or their specific orbital- and collisional histories. The higher σ in T_0 of the Earth indicates that it collected material with a wider range of temperatures than that accreted by Vesta. This result is consistent with dynamical models that predict that larger bodies accumulate material from a broader range of heliocentric distances than do smaller ones[2,3]. On this basis, we propose that the Earth did not accrete from chondrites alone, but instead stochastically from a summation of smaller precursor bodies,

[1]Institute of Geochemistry and Petrology, ETH Zurich, Zurich, Switzerland. [2]Institut für Geophysik, Ludwig-Maximilians-Universität München, Munich, Germany. [3]Department of Earth and Environmental Sciences, Michigan State University, East Lansing, MI, USA. [4]Laboratoire Lagrange, UMR7293, Université de Nice Sophia-Antipolis, CNRS, Observatoire de la Côte d'Azur, Nice, France. [5]School of Earth, Atmosphere and Environment, Monash University, Melbourne, Victoria, Australia. ✉e-mail: paolo.sossi@erdw.ethz.ch
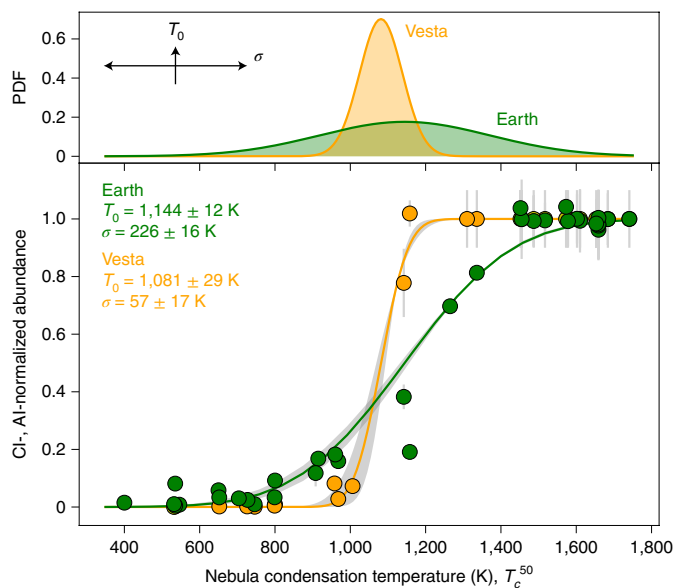
Fig. 1 | Fits to the bulk compositions of the mantles of the Earth and Vesta. CI-, Al-normalized abundances (f_i) and 1σ uncertainties (error bars) of lithophile elements in the BSE[6] (green) and Vesta[75] (yellow) plotted as a function of their 50% nebular condensation temperatures[22], with Si, Na, K, Zn and Cl updated from ref. [76]. Both bodies have abundances that approximate a cumulative normal distribution (equation (1)). The corresponding probability distribution function (PDF) is shown above. The curves (and their grey shaded 1σ error envelopes) were determined by a least-squares fit to error-weighted elemental abundances, $\chi^2 = \left([f_i - \bar{f}_i]/s_i\right)^2$ where $\bar{f}_i$ is the modelled value and s_i its 1σ uncertainty (Supplementary Table 2). The best-fit values of T_0 and σ are listed on the plot and yielded r.m.s. deviations of 0.071 ($n = 35$) for the Earth and 0.028 ($n = 25$) for Vesta. Manganese falls below the trend for the Earth's mantle, probably owing to partial incorporation into the Earth's core[77]. The linear scale highlights the gradual elemental depletion with T_c^{50} in the BSE, arguing against scenarios in which the Earth formed by mixing of two components (85% volatile-poor; 15% volatile-rich)[29,78]. A log-scale version of Fig. 1 is shown in Supplementary Fig. 3.

each with Vesta-like step-function element abundance patterns (σ tends to 0) and variable T_0 that reflect the temperatures at which they formed.

To quantitatively test this hypothesis, we examined four different N-body simulations[17] of the 'Grand Tack' scenario that reproduce the approximate number, masses and semi-major axes of the terrestrial planets. In this class of models, the migration of Jupiter, first inwards, then outwards owing to its resonant interaction with Saturn, clears the region between 3 and 6 au of planetesimals and embryos, and scatters them into the inner disk between 0.7 and 3 au, leaving a remnant population of planetesimals in the asteroid belt and beyond 6 au (refs. [17,18]) (Table 1). Any other dynamical model resulting in a comparable radial distribution of accreted material (Extended Data Fig. 1) would give equivalent results.

The sensitivity of the chemical and isotopic make-up of the Earth analogue to the compositional model, described below, was evaluated by performing 1,000 Monte Carlo simulations with three free parameters for each N-body run (Methods). It was assumed that all precursor bodies formed at the same time, meaning that their initial temperature (T_0) reflected their heliocentric distance, d, and was calculated according to the radial temperature profile of a high-opacity nebular midplane, $T_{midplane}$, set by the disk in steady-state mass accretion[19,20] (Extended Data Fig. 2):

$$T_0 = T_{midplane} = \left(\frac{9\tau GM_\odot \dot{M}}{64\pi\sigma_B d^3}\right)^{\frac{1}{4}}, \qquad (2)$$

where τ is the optical depth at the midplane (Methods), G is the universal gravitational constant, $M_\odot$ is the mass of the Sun and σ_B the Stefan–Boltzmann constant. The mass accretion rate to the Sun, ($\dot{M}$), the first free parameter, was varied randomly within a normal distribution of (1 ± 0.25) (1σ) $\times 10^{-7} M_\odot$ yr^{-1}. Observations of T-Tauri stars show that $\dot{M}$ (in $M_\odot$ yr^{-1}) decays as a function of time, t (Myr)[21]:

$$\log\left(\dot{M}\right) = -8.00 \pm 0.10 - (1.40 \pm 0.29)\log(t), \qquad (3)$$

indicating the time of planetesimal or embryo formation. Given $T_{midplane}$, planetesimals contain CI-normalized abundances (f_i) of 30 fictive elements, defined with T_c^{50} (at 10^{-4} bar) ranging from 350 to 1,800 K at 50 K intervals (Methods):

$$f_i = x_{i,body}/x_{i,Cl}, \qquad (4)$$

Fictive elements render the models independent of uncertainties or revisions in T_c^{50} of real elements[22,23], and permit quantification of systematic trends in their behaviour. If $T_{midplane} > T_c^{50}$ of element i, $f_i = 0$, otherwise, $f_i = 1$, defining a step-function abundance pattern in planetesimals. This distribution reflects their thermodynamic properties that result in their perfect retention or evaporation[14] and the inability of small (<1,000 km) bodies to retain an atmosphere[24]. The embryos comprise numerous planetesimals, each with a $T_{midplane}$ sampled normally about the $T_{midplane}$ of the embryo with a standard deviation, σ_{embryo} (see equation (1)). This, the second free parameter, has a mean of 87 K with a standard deviation of 24 K (1σ) and changes the smoothness of embryo compositions. This temperature range equates to a feeding zone width[25] of roughly ± 0.1 au for an embryo forming at 1 au.

To assess the extent to which partial evaporation (and hence isotopic fractionation) occurs during planetary accretion, the model computes a surface temperature increase in each body experiencing an impact that is proportional to the kinetic energy imparted by that impact (Methods). Each fictive element vaporizes with a partial pressure determined by its thermodynamic properties, with more volatile elements evolving higher partial pressures (Methods). Given the surface atmospheric temperature and pressure, the temperature–pressure profile of a convective atmosphere with height following the dry adiabat was determined, before transitioning to an isothermal region above the homopause[26]. Elements in the atmosphere may be lost to space via Jeans and hydrodynamic escape. Which regime prevails depends on the escape parameter (Extended Data Fig. 3):

$$\lambda_{esc} = \frac{v_{esc}^2 m_i}{2k_B T_{esc}}, \qquad (5)$$

where v_{esc} is the escape velocity of the body ($= \sqrt{2GM_{body}/r_{body}}$) M_{body} and r_{body} are its mass and radius, respectively, k_B is the Boltzmann constant, T_{esc} is the temperature at the escaping surface and m_i is the mean atmospheric mass. The value of m_i, the third free parameter, was sampled randomly from a normal distribution with a mean of 33.5 g mol^{-1} and $\sigma = 3.5$ g mol^{-1}, with limits corresponding to 23 g mol^{-1} (Na) and 44 g mol^{-1} (SiO). Jeans escape occurs for $\lambda_{esc} > 3$, whereas hydrodynamic escape prevails for $\lambda_{esc} < 3$ (Methods)[27]. Escape by other, non-thermal processes such as photoevaporation or ionization is neglected. Escape fluxes were calculated at 10 K steps, assuming grey-body cooling of the atmosphere (Methods). The composition of the residue was recomputed at each cooling step, assuming that element abundances equilibrated in the entire body.

Table 1 | Input parameters and final masses and semi-major axes of the analogue planet of the Earth resulting from the *N*-body simulations

Simulation	Embryos (0.7–3 au)		Planetesimals (0.7–3 au)		Planetesimals (6–8 au)		Earth Analogue	
	Mass (M_E)	n	Mass (M_E)	n	Mass (M_E)	n	Mass (M_E)	Semi-major axis (au)
GT/8:1/0.025/R2	0.025	212	3.81×10^{-4}	1,750	3.81×10^{-4}	500	1.107	0.936
GT/4:1/0.025/R7	0.025	170	3.81×10^{-4}	2,783	4.67×10^{-5}	1,563	0.957	0.907
GT/4:1/0.05/R8	0.050	87	3.81×10^{-4}	2,836	5.15×10^{-5}	1,563	0.937	0.969
GT/8:1/0.08/R18	0.080	67	3.81×10^{-4}	1,750	3.45×10^{-4}	500	1.074	1.179

The naming convention of *N*-body simulations includes (1) the Grand Tack (GT) model, (2) the mass ratio of embryos:planetesimals, (3) the mass of embryos in Earth masses (M_E) and (4) the run number with those parameters[18], separated by forward slashes.

Results

**Temperatures of precursor bodies set by a heliocentric gradient.** In all simulations, refractory elements accreted in concert with the total mass of the Earth analogue (Fig. 2 and Extended Data Fig. 4) because they were present in all planetesimals and were unaffected by atmospheric losses. By contrast, more volatile elements lagged behind their refractory counterparts. Simulations with high atmospheric loss rates (low m_i) were indistinguishable from cases in which atmospheric escape was suppressed (high m_i), meaning that the differential timing of volatile accretion depended only on precursor body compositions set by the value of $\dot{M}$ and d.

Our results indicate that while the proto-Earth analogue accreted ~80–90% of its final total mass by 25–100 Myr, only ~50% of the most volatile elements ($T_c^{50} < 500$ K) accreted within this timeframe. This reflects the preferential accretion of volatile-undepleted (that is, CI-like) planetesimals from beyond 6 au later in the Earth analogue's growth. Late accretion of this material (for example, during a giant impact) provides a physical explanation for the requirement that volatile-rich material constituted the final ~10 % of the Earth's mass and accreted after 30 Myr to explain the Earth's carbonaceous chondrite-like $^{107}Ag/^{109}Ag$ ratio and to reconcile Hf–W and Pd–Ag ages[28].

Once fully accreted, modelled elemental abundances in the Earth analogue adhered to a gradual decline with decreasing T_c^{50} that parallel observations (Fig. 3a,b), independent of the specific *N*-body simulation (Extended Data Fig. 5). Although a constant-abundance plateau was observed in some simulations, it extended only to elements with $T_c^{50} < 450$ K, and never up to 750 K or 1,000 K as suggested in recent models[16,29,30]. Monte Carlo simulations indicated that the composition of the Earth analogue depended strongly on $\dot{M}$ but was nearly independent of σ_{embryo} and m_i (Extended Data Fig. 6). Therefore, its final composition was inherited from its precursors, rather than modified subsequently by partial evaporation during collisions.

In the model, the elongated (high-σ) shape in the BSE arose from the summation of precursor bodies with a wide range of $T_{midplane}$, which, for a given $\dot{M}$, is related to heliocentric distance (Extended Data Fig. 2). This followed from the condition applied to planetesimals that $f_i = 0$ when $T_{midplane} > T_c^{50}$, which became increasingly probable as T_c^{50} decreased. Even though planetesimals initially had step-function patterns, this process produced a smooth pattern in the BSE by the central limit theorem. The corollary is that step-function patterns (low-σ) should be more evident in smaller bodies that form in local feeding zones, in which precursors have a restricted range of $T_{midplane}$, as observed for Vesta[14] (Fig. 1).

The best fits to the lithophile elemental abundances in the BSE were determined by minima of the root mean squared (r.m.s.) deviation of model Earth analogues from the data (Fig. 3 and Extended Data Fig. 5). The r.m.s. deviation was minimized for $\dot{M} = 1.08 (\pm 0.17, 1 \text{ au}) \times 10^{-7} M_\odot \text{ yr}^{-1}$ (Extended Data Fig. 6)
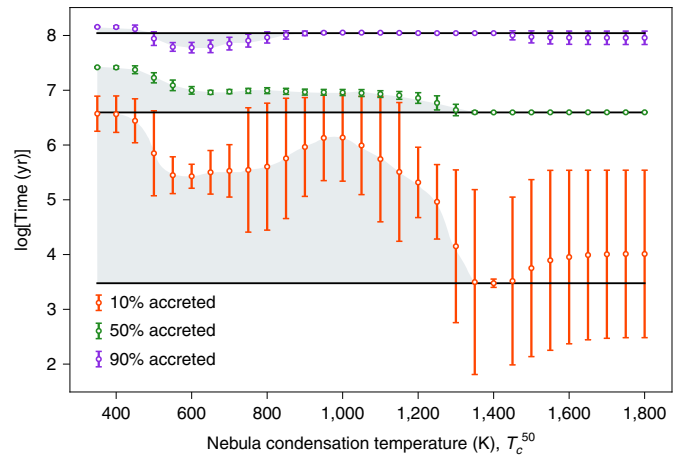
Fig. 2 | Timing of element accretion to the Earth as a function of volatility. Points represent the time in the GT/4:1/0.05/R8 *N*-body simulation (ordinate) at which a given element (abscissa) reaches a threshold value (10%, 50% or 90%) of its final abundance. These points are the per cent accreted $= 100 \times (x_i M)_{t_t} / (x_i M)_{t_f}$, where the subscripts t and f denote the threshold time and the final time, respectively, and M is the mass of the growing Earth analogue. Error bars (1σ) denote the range given by Monte Carlo models for different $\dot{M}$, σ_{embryo} and m_i across the 1,000 simulations. The lack of an error bar indicates that the element reached the given per cent accreted value at the same time in each Monte Carlo simulation. The mass of the Earth analogue, M_t/M_f, through time is delineated by horizontal lines at 10%, 50% and 90%. Offset between these lines and the coloured points is the differential accretion time, denoted by the grey shaded fields. The large error bars on refractory elements arise from their dilution/enrichment in planetesimals and embryos with/without the more abundant elements with T_c^{50} near 1,350 K (Supplementary Table 1). Equivalent plots for the four *N*-body simulations are shown in Extended Data Fig. 4.

and was insensitive to the specific accretion history in the subset of the four *N*-body simulations investigated here. Assuming gradual, rather than step-like, patterns for planetesimals (as per those of embryos) did not change the best-fit value of $\dot{M}$. These mass accretion rates yielded $T_{midplane} = 1,410 \pm 60$ K at 0.7 au, coinciding with the T_c^{50} of the major rock-forming elements, Mg, Si and Fe (ref. [22]).
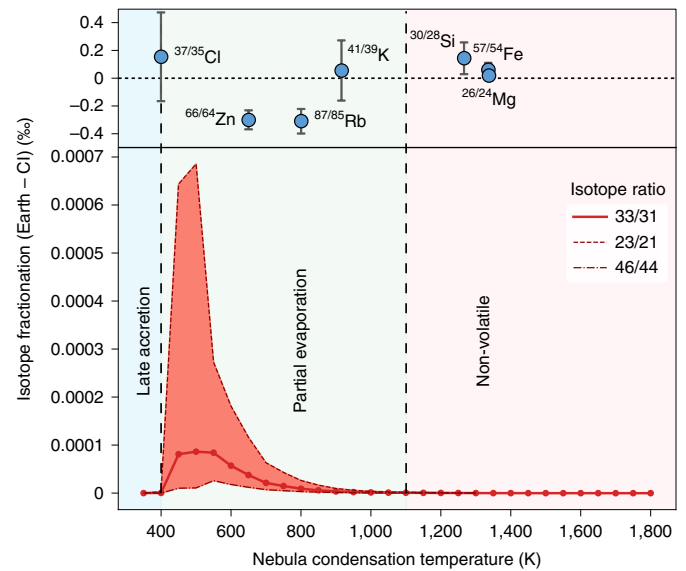
Observations of T-Tauri stars show that younger disks have faster mass accretion rates than do older ones[31] (equation (3)). By analogy, accretion rates of ~$10^{-7} M_\odot \text{ yr}^{-1}$ indicate rapid establishment, ~0.2 ± 0.1 Myr, of the compositional architecture of the inner disk within the lifetime of the nebular gas. Detailed numerical models also support the early formation of planetesimals in the inner disk by ~0.5 Myr (ref. [32]) or ~1 Myr (ref. [33]). Moreover, this timescale matches volatile depletion ages based on Rb–Sr and Mn–Cr
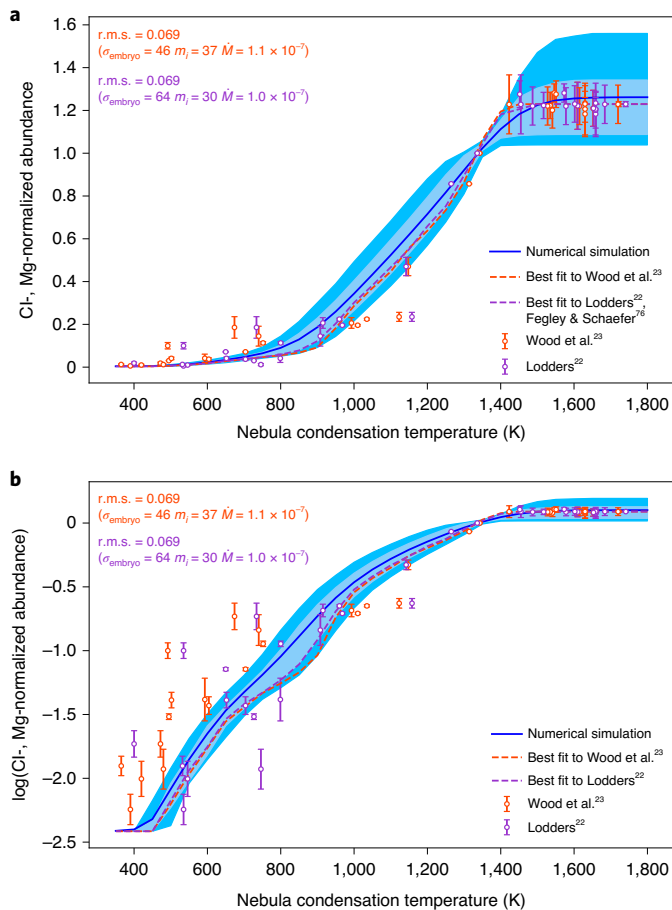
Fig. 3 | Elemental abundances modelled in the fully accreted Earth analogue relative to observations. a,b, CI-, Mg-normalized elemental abundances in the BSE with their 1σ uncertainties [6] as a function of their 50% nebula condensation temperatures according to Wood et al.[23] (red); and Lodders[22] with updates from Fegley and Schaefer[76] as per Fig. 1 (purple) compared with abundances predicted by 1,000 Monte Carlo simulations per N-body simulation (here GT/4:1/0.05/R8; see Extended Data Fig. 5 for others) plotted on linear (**a**) and logarithmic (**b**) scales. The average composition over 1,000 runs is shown by the solid blue line with the percentile ranges of the simulations (25th to 75th, light blue shading and 10th to 90th, dark blue shading). The dashed lines show the simulations that minimized the r.m.s. deviation from the data. The r.m.s. values are listed in the top-left corner, along with those of the three random variables to which they correspond. Only lithophile elements were plotted, as siderophile elements are further depleted by core formation, which was not considered in our model.

Fig. 4 | Stable isotope fractionation modelled in the fully accreted Earth relative to observations. Top: isotopic fractionation for elements for which the difference between Earth and CI chondrites is well-constrained, Cl[43], Zn[7], Rb[10], K[8], Si[37], Fe[38] and Mg[39], together with their 1σ uncertainties (error bars). Bottom: results for the GT/4:1/0.05/R8 N-body simulation, where the red line indicates the mean isotopic fractionation (in ‰ relative to the initial value; that is, CI chondrites) across 1,000 Monte Carlo runs in the Earth analogue. The isotope ratios (in g mol^{-1}; (m_i = numerator isotope, $\Delta m_i = 2$ atomic mass units) are listed in the legend. The vertical dashed lines delimit zones pertaining to late accretion (volatile elements whose isotopes are present in chondritic ratios), partial evaporation (elements that bear an isotopic signature of partial evaporation during atmospheric loss) and non-volatile (elements that were not lost and remain chondritic). The scale of isotopic variation observed exceeds that produced in the Monte Carlo runs, except for low-m_i runs in the GT/8:1/0.025/R2 N-body simulation (Extended Data Fig. 7). The observations do not follow the behaviour expected for partial evaporation either, which generates heavy isotope ratios for elements with $450\,K < T_c^{50} < 800\,K$. Equivalent plots for the four N-body simulations are shown in Extended Data Fig. 7.

systematics of small differentiated bodies (<1.5 Myr; refs. [34,35]) and of the Earth (1–2 Myr; ref. [36]). Subsequent, post-nebular orbital evolution produces its smooth (high-σ) pattern over longer timescales, nearing ~10^8 yr.

The stable isotope composition of the Earth represents the sum of contributions from partial evaporative losses and accretion of unevaporated materials. The isotope fractionation evolved is proportional to the amount of the element lost and the isotopic fractionation factor. In the N-body simulations, isotope ratios for each element in planetesimals and embryos were initially CI chondritic, and atmospheric escape was calculated for all bodies that experienced a collision. In the fully accreted Earth analogue, a peak was observed in elements with $450\,K < T_c^{50} < 800\,K$ across all simulations (Fig. 4 and Extended Data Fig. 7). These elements were not

sufficiently volatile to have been lost completely (and thus prone to overprinting by late-accreted material), but still volatile enough to record partial evaporation over accretion. The magnitude of isotope fractionation in the fully accreted Earth analogue was proportional to $1/m_i$ (Fig. 4 and Extended Data Fig. 8).

Such isotope fractionation patterns are explicable through the dynamics of planetary impacts. The tendency for atmospheric loss (and hence isotope fractionation) to occur was quantified by λ_{esc} (equation (5)). As the Earth analogue grew, λ_{esc} gradually increased, upon which were superimposed embryo collisions ($M_E > 0.05$) that produced transient decreases in λ_{esc} via impact heating (Extended Data Fig. 3), during which atmospheric loss was most pronounced. For any given N-body simulation, there were typically one to two collisions that induced hydrodynamic escape. These events were restricted to the nascent stages of the Earth analogue's formation, during which its mass was ~0.05 to 0.2 M_E (Extended Data Fig. 3). Although temperatures in later, giant impacts may be higher, the proclivity for atmospheric loss was offset by the larger escape velocity, as λ_{esc} depends on v_{esc}^2, but only on $1/T$ (equation (5)).

As such, chemical and isotopic fractionation generated by early, high-energy events were readily overprinted by accretion thereafter. The most volatile elements were delivered late by material that had seen no evaporation, and hence had chondritic isotope ratios (Fig. 4). The isotope composition of elements with $450\,K < T_c^{50} < 800\,K$

depended largely on the Earth analogue's accretion path and hence the N-body simulation. A small fraction (<5%) of runs with the lowest m_i in the most energetic simulation, GT/8:1/0.025/R2, reached 3‰ (Extended Data Figs. 7 and 8). For all other runs, the limited degree of isotopic fractionation was consistent with the observed <0.4% (refs. [7–10]) deviation of the BSE from CI chondrites in K (~1,000 K), Rb (~800 K), Zn (~700 K) and Cl (~400 K) isotope compositions (Fig. 4). Therefore, partial atmospheric escape from large bodies ($\geq 0.2\,M_E$) had minimal influence on the final compositional and isotopic make-up of the Earth. By extension, isotopic variations of less volatile elements, including Mg, Fe and Si[37–39] (Fig. 4) were unlikely to originate from partial evaporation of embryos. Instead, they could have been inherited earlier from nebular condensation[37] or planetesimal evaporation[40]. In this manner, the BSE would have inherited near-chondritic isotope ratios in volatile elements whose abundances are depleted with respect to CI chondrites. Nevertheless, consideration of the specific thermodynamic properties of these elements over a wider range of N-body simulations is required. Conversely, the isotopic imprint of atmospheric loss was more readily preserved on small bodies for which escape was both more pronounced and less overprinted by continued accretion, consistent with enrichment in heavy isotopes of K, Cl and Zn of the Moon and Vesta[41–43].

Temperatures of precursor bodies set by radiogenic heating. Aluminium-26, which decays to ^{26}Mg (half-life $t_{1/2} = 0.7$ Myr), was abundant enough to have caused melting and vaporization on small rocky bodies, provided they formed sufficiently early (≤ 2 Myr)[44]. Therefore, a variation on the stochastic accretion hypothesis arises if the temperatures of precursor bodies reflect ^{26}Al decay in addition to, or (in the extreme case) instead of, the smooth heliocentric decrease in disk temperature modelled above. The end-member case was investigated by randomly assigning each body an initial temperature selected from a normal distribution with mean, $T_0 = 1,000 (\pm 50, 1\sigma)$ K and standard deviation, $\sigma = 175$ K (Extended Data Fig. 5). T_0 could reach ~1,600 K, consistent with numerical models[45], and replaced $\dot{M}$ as the first random variable in the Monte Carlo simulations. The remainder of the simulation was identical to that described above.

This initial temperature distribution also explains the abundance pattern of the BSE (Extended Data Fig. 9). However, because the compositions of planetesimals were independent of heliocentric distance, there was no systematic distinction in the accretion times of volatile and non-volatile elements, a result that contravenes evidence from the Pd–Ag and Hf–W systems[28]. This inconsistency can be resolved should planetesimals have accreted more slowly with increasing heliocentric distance, causing the effects of ^{26}Al heating to diminish[33,44]. In this scenario, a planetesimal population in the inner disk formed at 0.6–1.3 Myr (ref. [33]). Therefore, ^{26}Al heating can perturb the thermal structure imposed by the disk, and also produces the chemical and isotope composition of Earth by stochastic accretion, provided a heliocentric gradient in composition is present.

Growth of the Earth by pebble accretion. The formation of the Earth via pebble accretion (the growth of planetary objects by centimetre-sized pebbles dragged aerodynamically with the inward-migrating nebular gas), a popular alternative mechanism for planetary growth[46], was simulated by prescribing a mass accretion rate that scaled with $M_E^{2/3}$, typical of two-dimensional pebble accretion in the Hill regime[47]. Pebble fluxes were assumed to mirror mass accretion rates to the Sun (equation (3)) and resulted in the growth of the model Earth to $0.9\,M_E$ in 3.85 Myr, consistent with disk accretion models (~5 Myr; ref. [5]). Pebbles initially formed at the snow line[4] and subsequently drifted inwards by interactions with the surrounding nebular gas. Because pebbles are small, they thermally equilibrate with the gas at 1 au, whose temperature was calculated over time with equations (2) and (3). Thus, elemental abundances in pebbles at the time of their accretion by the Earth were determined as per planetesimals, but using the temperature at 1 au as T_{midplane}.

As pebbles accrete continuously in time, the model Earth's surface reached only modest temperatures compared with planetesimal accretion, ~1,750 K, sufficient to melt and vaporize the pebbles. However, the escape of vaporized material occurs in the upper atmosphere, near the Hill radius, or deeper, at the Bondi radius, if the Earth were still embedded in the disk[48]. At these locations, temperatures drop to ~400 to 100 K (ref. [5]), meaning elements with $T_c^{50} > 400$ K are solids. Consequently, atmospheric loss and isotopic fractionation is muted (Extended Data Fig. 10). Pebble accretion models produced concave-down patterns that declined at T_c^{50} lower than observed in the BSE (Extended Data Fig. 10). This resulted from the dependence of the accretion rate on $M_E^{2/3}$, meaning that the majority (85%) of the model Earth's mass accreted between 1 and 3.85 Myr, when temperatures at 1 au were ≤ 500 K (Extended Data Fig. 10). As such, the depletion of elements with T_c^{50} above this temperature was limited. Therefore, unless the pebbles themselves were already impoverished in volatile elements, pebble accretion alone did not produce the volatile depletion pattern of the Earth.

Discussion

The distribution of initial temperatures, and hence the compositions of the accreted planetesimals and embryos, controlled the composition of the Earth. To achieve sufficient temperatures in these precursor bodies, either by heating in the disk and/or ^{26}Al decay, they must have formed by ~1 Myr, a timescale that is consistent with radiometric ages for volatile depletion[34,36] and protoplanetary disk models[32,33]. Whether precursor body compositions were set by nebular condensation or planetesimal evaporation could be discriminated by holistic models of the growth of planets from the dust to embryo stages. In the context of the Grand Tack model, and other models in which the Earth accreted from a radial distribution of material (Extended Data Fig. 1), some form of heliocentric temperature gradient was necessary to explain the late accretion of volatile-rich bodies (Fig. 2) that satisfied the near-chondritic radiogenic[28] and stable[7–10] (Fig. 4) isotope composition of volatile elements in the Earth.

The mean volatile content of a planet, quantified by its T_0, is expected to increase with heliocentric distance. Should a heliocentric gradient have been established by disk accretion, then a continuous decrease in T_0 of the terrestrial planets would be observed, whereas ^{26}Al heating may produce a dichotomy in the compositions of inner and outer Solar System planetesimals owing to their differential formation times. As they grow, planets accrete material from an expanding range of heliocentric distances[2,3]. This translates into a greater distribution of T_0 in precursor bodies, implying that larger planets should have more gradual depletion patterns (high σ) than smaller ones (low σ) (Fig. 1). Moreover, smaller planets are more likely to preserve isotopic imprints of atmospheric loss, resulting in heavy stable isotope compositions of volatile elements relative to their building blocks. Potassium isotopes in the Earth, Mars, the Moon and Vesta bear out this expectation, as they become increasingly non-chondritic with decreasing planetary mass[49]. The compositions of the terrestrial planets, together with their masses and heliocentric distances, offer the means by which to test these predictions.

Methods

N-body simulations. N-body simulations proceeded by perfect-merger impacts that resulted in a net increase in mass of larger bodies at the expense of smaller ones (oligarchic growth) to produce three to four terrestrial planets with masses and semi-major axes close to those observed at the present day[17].

We performed four simulations, labelled GT/4:1/0.05/R8, GT/4:1/0.025/R7, GT/8:1/0.08/R18 and GT/8:1/0.025/R2; see Table 1 for the masses and distributions of embryos and planetesimals, and refs. [17,18] for a detailed description of the simulations.

Disk structure and initial composition. All bodies (embryos and planetesimals) were assigned an average density of 3,000 kg m^{-3}. They were prescribed to initially contain some fraction of the CI-normalized abundances (f_i) of 30 fictive elements (i) defined with T_c^{50} (at 10^{-4} bar total pressure) ranging from 350 to 1,800 K at 50 K intervals, where:

$$f_i = x_{i,\text{body}}/x_{i,\text{initial}}, \tag{6}$$

and x corresponds to the mole fraction. Where $x_{i,\text{body}} = x_{i,\text{initial}}$, the body had its full complement of i, and was equivalent to a CI-chondritic composition. The initial temperature of the planetesimal or embryo was determined by d. The temperature profile of a high-opacity nebular midplane in steady-state mass accretion is[19,20]:

$$T_{\text{midplane}} = \left(\frac{9\tau GM_\odot \dot{M}}{64\pi\sigma_B d^3} \right)^{\frac{1}{4}}, \tag{7}$$

where τ is given by $\tau = \kappa \Sigma / 2$ (ref. [50]), where κ is the Rosseland mean opacity ($\sim$0.3 m^2 kg^{-1} in the range 100–1,500 K; ref. [51]) and $\Sigma = 3,500(\dot{M}/10^{-8})d^{-3/4}$ in kg m^{-2} (d in au) is the surface density of the gas suitable for the optically thick accretion phase of the star, $\dot{M} > 10^{-9} M_\odot$ yr^{-1}, in the planet-forming region[20,52]). $\dot{M}$ was the first random variable for the Monte Carlo simulations (see 'Monte Carlo simulations').

We impose the constraint that, for planetesimals, if $T_{\text{midplane}} > T_c^{50}$ of element i, $f_i = 0$, otherwise, $f_i = 1$, defining a step-function pattern. As embryos are larger bodies, they themselves are expected to comprise planetesimals with step functions. Hence, abundances in the embryos reflected the summation of a number, $N = (M_{\text{embryo}}/M_{\text{planetesimals}})$ of planetesimals, each with a T_{midplane} sampled normally about the T_{midplane} of the embryo, with standard deviation σ_{embryo}. If σ_{embryo} was low, the depletion pattern in the embryo was closer to a step function, whereas high σ_{embryo} led to a smoother curve. σ_{embryo} was the second random variable for the Monte Carlo simulations (see 'Monte Carlo simulations').

Energy budget during impact heating and cooling. Collisions result in a temperature increase according to the conversion of kinetic energy to heat. The energy released upon the impact of two bodies of masses M_A and M_B travelling at velocities v_A and v_B, respectively, is the sum of their kinetic energies, E_k:

$$E_k = \frac{1}{2}M_A v_A^2 + \frac{1}{2}M_B v_B^2. \tag{8}$$

However, only a fraction of the total kinetic energy is converted into heat, depending on the characteristics of the impacting material and obliquity and mass of the impact[53,54], while the heated region depends on the amount of energy transmitted beyond the isobaric core of the body. These poorly known terms were consolidated into a single empirical constant, h, which was set to 0.5 (ref. [55]). The temperature increase is the total heat distributed throughout the affected mass, divided by the heat capacity of the material C_p:

$$\Delta T = \frac{h}{C_p} \left(\frac{E_k}{M_{\text{planet}}} - \Delta H_{\text{fus}} - \Delta H_{\text{vap}} \right) = \frac{h}{C_p} \left(\frac{v_{\text{imp}}^2}{2} - \Delta H_{\text{fus}} - \Delta H_{\text{vap}} \right). \tag{9}$$

Where p is pressure and C_p is that for molten peridotite near its liquidus (1,800 J kg^{-1} K^{-1}; ref. [56]), M_{planet} is the final mass of the planet, and v_{imp} is the impact velocity given in the N-body simulation. Temperature increased if the energy delivered was in excess of the latent heat of fusion ($\Delta H_{\text{fus}} = 4 \times 10^5$ J kg^{-1} at 1,400 K; ref. [57]), then vaporization ($\Delta H_{\text{vap}} = 5 \times 10^6$ J kg^{-1} at 2,000 K; ref. [55]) and finally an upper limit at 6,000 K, whereupon behaviour became supercritical[58,59]. The mass of material that experienced peak temperatures (the isobaric core) scaled with impactor radius[39,55]. However, because N-body simulations represent a swarm of planetesimal impacts, the heated area was likely to have been uniformly distributed in the body.

Following heating to maximum temperatures, the planetary body cools by a combination of black body radiation, latent heat of vaporization and gravitational potential energy, with the energy balance given by[60]:

$$\frac{dT}{dt} = \frac{\left(\frac{dm}{dt} \left(\frac{GM_{\text{planet}}}{r} + \Delta H_{\text{vap}} \right) + 4\pi r^2 \sigma_B \epsilon T_s^4 \right)}{M_{\text{planet}} C_p}. \tag{10}$$

The contribution of the evaporative cooling and escape term, $\frac{dm}{dt}\left(\frac{GM_{\text{planet}}}{r} + \Delta H_{\text{vap}} \right)$, was small and was neglected. Here r is the planetary radius (assuming a radiating atmosphere from the surface) and T_s the surface temperature. The emissivity, ϵ, takes into account that planets are not perfect black bodies, and was set to 0.05 to replicate cooling timescales for terrestrial planets with thick atmospheres[61–63].

Temperature was calculated at 10 K cooling intervals throughout the simulation. This temperature was then fed in as an input to calculate the composition of the atmosphere (see 'Vapour pressure'), its subsequent loss at each temperature step ('Atmospheric loss') and thus to recalculate a new bulk composition ('Compositional evolution') in a loop.

Vapour pressures. For silicate materials, vaporization reactions can be generalized as:

$$M^{x+n}O_{\frac{x+n}{2}} (l) = M^x O_{\frac{x}{2}} (g) + \frac{n}{4} O_2 (g), \tag{11}$$
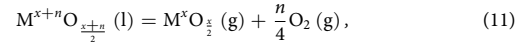
where $M^{x+n}O_{\frac{x+n}{2}}$ is the metal oxide species in the silicate melt, $M^x O_{\frac{x}{2}}$ is the stable gas species with metal oxidation state of x, balanced by $\frac{n}{4}$ moles of O_2 gas for a congruent reaction (that is, a reaction in which the gas(es) produced have the same composition as the reactant(s)).

At equilibrium, the partial pressure (assuming ideal gas behaviour such that $f = p$) is given by:

$$p\left(M^x O_{\frac{x}{2}} \right) = \frac{K_{(r)} X\left(M^{x+n}O_{\frac{x+n}{2}} \right) \gamma \left(M^{x+n}O_{\frac{x+n}{2}} \right)}{f_{O_2}^{n/4}}, \tag{12}$$

where X is the mole fraction and γ is the activity coefficient. The equilibrium constant of reaction, $K_{(r)}$, is given by:

$$K_{(r)} = \exp\left(\frac{-\Delta G_{(r)}}{RT_s} \right), \tag{13}$$

for which $\Delta G_{(r)}$ is the Gibbs free energy change of the vaporization reaction, R the gas constant and T_s the equilibrium temperature set by the magma ocean at its surface in Kelvin. At low pressures at which volume changes are small relative to those of the standard state (here taken at 1 bar):

$$\Delta G = \Delta H - T_s \Delta S \tag{14}$$

In which ΔH is the enthalpy change and ΔS is the entropy change of the reaction. Substituting this equation into equation (12), one obtains:

$$\log p\left(M^x O_{\frac{x}{2}} \right) = \left(\frac{-\frac{\Delta H}{T_s} + \Delta S}{2.303R} \right) + \log\left(\frac{X\left(M^{x+n}O_{\frac{x+n}{2}} \right) \gamma \left(M^{x+n}O_{\frac{x+n}{2}} \right)}{f_{O_2}^{n/4}} \right). \tag{15}$$

From experimental assessment of the equilibrium vapour pressures of metal-bearing gas species above metal oxides or metal oxide components in silicate melts, ΔS is near constant[14,64], which results in slopes in $\log p_i$ versus T space that are sub-parallel for almost all elements (Supplementary Fig. 1). Element volatilities were defined by their 50% condensation (or evaporation) temperature in the solar nebular gas[14]:

$$T_c^f = \frac{-\Delta H}{\left(R\left(\frac{n}{4}\ln f_{O_2} + \ln P_T + \ln \frac{f_{\text{vap}}}{(1-f_{\text{vap}})} \right) - \Delta S \right)}. \tag{16}$$

Here $f_{\text{vap}} =$ the fraction in the vapour (0.5 for 50% condensation). The f_{O_2} was that of a cooling solar nebula[65], while the total pressure was 10^{-4} bar, in keeping with convention[22,23]. The T_c^{50} of a given fictive element was defined by holding ΔS constant and changing the value of ΔH in equation (16). Their properties are shown in Supplementary Table 1.

The partial pressure was determined as a function of temperature, element activity, f_{O_2} of the atmosphere and the stoichiometry of the vaporization reaction, n (equation (11)). This linked the T_c^{50} of an element with its general volatility behaviour under planet-forming conditions. Because most elements evaporate according to $n = 2$ stoichiometries[14], including all five major cation-forming elements in the BSE composition (Fe, Mg, Si, Ca and Al), we adopted $n = 2$ for all fictive elements (Supplementary Table 1). Hence, relative fractionation by volatility was insensitive to f_{O_2}, which was not the case for the alkalis ($n = 1$), or for the Group VI metals (Cr, Mo and W) for which $n < 0$ (ref. [14]). However, this simplification is made to establish the overall trend of element depletion, and not to account for anomalies in the abundances of certain elements. Moreover, it is independent of any eventual revisions to T_c^{50} values.

The sum of the partial pressures dictated the total pressure at any given T and f_{O_2}:

$$P_T = \sum_{M^x O_{\frac{x}{2}} = i}^{i} p\left(M^x O_{\frac{x}{2}} \right), \tag{17}$$

since $p\left(M^x O_{\frac{x}{2}} \right)$ depends on $f_{O_2}^{-n/4}$, congruent evaporation (equation (11)) demands that the oxygen fugacity be equal to $n/4$ times the sum of the partial pressures of the metal oxide species. Because $n = 2$ in our treatment (Supplementary Table 1), then:

$$f_{O_2} = 0.5P_T = 0.5 \sum_{M^x O_{\frac{x}{2}} = i}^{i} p\left(M^x O_{\frac{x}{2}} \right). \tag{18}$$

Thus, the value of f_{O_2} was solved iteratively until the term $0.5P_T$ was equal to 1/2 the sum of the individual partial pressures of each component at a given temperature. Here we constrained element activities by fitting our value of P_T to that calculated for the evaporation of silicate mantles[66]. To do so, we assigned an activity to each fictive element as a function of its T_c[50]. In planetary materials, the three most abundant elements (Fe, Mg and Si) have T_c[50] $\approx 1{,}300$–$1{,}400$ K. We used a Gaussian distribution to model a peak element activity at about 1,350 K. The rate at which element activity declined was found by minimization to the P_T determined in ref. [66] over the range $1{,}800$ K $< T < 3{,}000$ K, using the objective function:

$$\chi^2 = \Sigma \left(P_T \, (\text{ref. 66}) - P_T \, (\text{calc}) \right)^2 . \tag{19}$$

By iterating the value of c:

$$(x_i\gamma_i)_{\text{initial}} = \frac{\exp\left(-\frac{(T_{c,i}^{50} - 1{,}350)^2}{2c^2}\right)}{\sum_i (X_i\gamma_i)_{\text{initial}}}. \tag{20}$$

We obtained a best-fit value to the total pressure above the BSE[66] (Supplementary Fig. 2) at $c = 100$, yielding the initial activities, $(x\gamma)_{\text{initial}}$, shown in Supplementary Table 1.

Atmospheric loss. Escape of the atmosphere was calculated self-consistently on the basis of its pressure–temperature structure. The total pressure at the surface, P_T, (equation (17)) was a direct result of T_s, given that any crustal boundary layer is likely to be approximately a few centimetres thick[39,67] and prone to foundering. Even for small bodies 1/2 the mass of Pluto, the evaporation rate quickly attained a steady state with loss rate, such that the surface pressure was that at equilibrium[40]. A rapidly convecting terrestrial magma ocean (viscosities ≈ 0.1 Pa s; ref. [68]) experienced turnover in days, meaning evaporation was not diffusion-limited by transport of material to the surface.

Throughout the Earth's accretion at any given temperature step, we modelled two thermal escape regimes, Jeans and hydrodynamic escape. Energy-limited or ionization-driven escape were not considered as they require knowledge of the solar energy flux. The prevailing mode of escape was determined by the competing influences of gravity and thermal energy, encapsulated in λ_{esc}[69]:

$$\lambda_{\text{esc}} = \frac{v_{\text{esc,exo}}^2 m_i}{(2k_B T_{\text{exo}})}, \tag{21}$$

where $v_{\text{esc,exo}}$ is the escape velocity of the planet at its exobase and T_{exo} is the temperature at the exobase; m_i is the third random variable for the Monte Carlo simulations (see 'Monte Carlo simulations'). Atmospheric structure was described by its scale height, H, the height over which its number density declined by a factor of $1/e$. For a well-mixed atmosphere, H was evaluated at the tropopause by:

$$H_{\text{trop}} = \frac{k_B T_{\text{trop}}}{m_i g_s} \left(\frac{r_{\text{trop}}}{r_s} \right)^2, \tag{22}$$

where

$$g_s = \frac{GM_{\text{planet}}}{r_s^2}, \tag{23}$$

where r_s is the radius at the surface, and r_{trop} is the radius at the tropopause ($r_{\text{trop}} = r_s + z_{\text{trop}}$, where z_{trop} is the height above the surface at the tropopause). Thus, the T_s and P_T set by evaporation at the surface need to be extrapolated upwards to the tropopause. This was achieved using the expression for a convective (dry adiabat), optically thin troposphere[26]:

$$T_{\text{trop}} = T_s \left(\frac{P_{T,\text{trop}}}{P_T} \right)^{\frac{R}{C_p}} . \tag{24}$$

Here C_p is the heat capacity of an ideal, complex gas at constant pressure ($= 4R$). For an optically thin atmosphere in the absence of external heat sources, the temperature tends to a constant value given by the 'skin temperature'[26] ($= T_{\text{trop}}$):

$$T_s = 2^{0.25} T_{\text{trop}}. \tag{25}$$

Combining equation (25) with equation (24) leads to $P_{T\text{trop}} = 0.5P_T$. This limit, the tropopause, defined the transition from the convective troposphere to the diffusive stratosphere that overlies it. The adiabatic expansion of an ideal gas in hydrostatic equilibrium as a function of height above the surface (z) is:

$$P_T(z) = P_T \exp\left(-\frac{z}{H_z} \right), \tag{26}$$

where z_{trop}:

$$z_{\text{trop}} = -\ln(0.5) H_{\text{trop}}. \tag{27}$$

As H_{trop} appears in both equation (27) and equation (22), these equations were resolved iteratively until they converged upon a unique value of z_{trop} and H_{trop}. Above this point, in the stratosphere, temperature as a function of z is constant, reflecting the skin temperature. The number density at the exobase, which was defined as the point at which the mean free path ($l = 1/n_{\text{exo}}\Omega$) equals the scale height (H_{trop}), is:

$$n_{\text{exo}} = \frac{1}{\left(H_{\text{trop}} \sqrt{2\pi\Omega^2} \right)}, \tag{28}$$

where Ω is the collision integral:

$$\Omega = 1.5 \times 10^{-10} m. \tag{29}$$

The escape velocity at the exobase was then calculated:

$$v_{\text{esc,exo}} = \sqrt{\frac{2GM_{\text{planet}}}{r_{\text{exo}}}} \tag{30}$$

Where the radius of the exobase is given by adiabatic expansion:

$$r_{\text{exo}} = r_s + z_{\text{exo}} = r_s - \ln\left(\frac{n_{\text{exo}}}{n_s} \right) H_{\text{trop}} \tag{31}$$

The number density at the surface was calculated by the ideal gas law:

$$n_s = \frac{P_T}{T_s k_B} \tag{32}$$

m_i was held constant throughout the simulation; λ_{esc} at the exobase of the body could then be evaluated. If $\lambda_{\text{esc}} > 3$, the position of the exobase was further out than the radius at which the gas exceeded the sound speed, and Jeans escape prevailed. In this regime, the mass loss rate (in molecules m^2 s^{-1}) is:

$$\frac{dn_i}{dt} \frac{1}{(4\pi r_{\text{exo},i}^2)} = 0.73 \frac{n_{\text{exo},i}}{2\sqrt{\pi}} \left(\frac{2k_B T_{\text{eff}}}{m_i} \right)^{0.5} (1 + \lambda_{\text{esc}}) \exp(-\lambda_{\text{esc}}) \tag{33}$$

or (in kg s^{-1}):

$$\frac{dm_i}{dt} = 2.92\pi r_{\text{exo},i}^2 \frac{n_{\text{ex},i}}{2\sqrt{\pi}} \left(\frac{2k_B T_{\text{eff}}}{m_i} \right)^{0.5} (1 + \lambda_{\text{esc}}) \exp(-\lambda_{\text{esc}}) m_i \tag{34}$$

If $\lambda_{\text{esc}} < 3$, the gas exceeded the speed of sound and a transonic outflow of the atmosphere resulted. The gas velocity was determined by T, P_T and the density (ρ) of its constituents at any given point, constrained by mass and momentum conservation[70]. At the 'sonic point', the velocity of the gas reached that of the speed of sound in the medium (c_s). For an ideal gas, c_s is given by:

$$c_s = \sqrt{\frac{\frac{7}{5} P_{T,\text{trop}}}{\rho_{\text{trop}}}} = \sqrt{\frac{\frac{7}{5} k_B T_{\text{trop}}}{m_i}}. \tag{35}$$

Where the factor 7/5 is the value of the adiabatic index for a diatomic gas (five degrees of freedom), and accounts for the heat of compression. The sonic point, or Bondi radius, is:

$$r_B = \frac{GM_{\text{planet}}}{2c_s^2}. \tag{36}$$

The hydrodynamic mass loss rate depends on the density of the gas phase at r_B. To estimate this value, the pressure of the gas at the surface was integrated outwards to r_B. For an adiabatically expanding gas, the relation is:

$$P_{r_B} = P_T \exp(-(r_B - r_{\text{planet}})/H_{r_B}) \tag{37}$$

The number density (in units of atoms per m^3) at the sonic point is:

$$n_{r_B,i} = P_{r_B}/k_B T_{r_B} \tag{38}$$

The molecular loss rate (molecules s^{-1}) is then:

$$\frac{dn_i}{dt} = 4\pi r_B^2 n_{r_B,i} c_s \tag{39}$$

or (in kg s^{-1}):

$$\frac{dm_i}{dt} = 4\pi r_B^2 n_{r_B,i} c_s m_i \tag{40}$$

To estimate isotopic fractionation during atmospheric loss, two simulations were run concurrently by varying m_i (which is a bulk property of the atmosphere

in the model framework and could not be independently varied for each element) according to:

$$m_j = m_i + (i - j) \times 1.67 \times 10^{-27} \text{ kg} \tag{41}$$

Here, the quantity $(i-j)$ was set to 2, reflecting the isotopic mass difference between most common systems (for example, ^{66}Zn/^{64}Zn; ^{30}Si/^{28}Si, ^{41}K/^{39}K). The scale heights of both isotopes, i and j, were calculated independently, such that equation (22) became:

$$H_{\text{trop}} = \frac{k_B T_{\text{trop}}}{m_j g_s} \left(\frac{r_{\text{trop}}}{r_s} \right)^2 \tag{42}$$

simulating the separation of two isotopes by their scale heights in the stratosphere. Therefore, both hydrodynamic and Jeans escape could cause isotope fractionation. The Jeans escape rate was further modified owing to the dependence of the relative mass loss rate dm_i/dm_j on $(m_j/m_i)^{0.5}$. As such, equation (33) became:

$$\frac{dn_j}{dt} \frac{1}{(4\pi r_{\text{exo}}^2)} = 0.73 \frac{n_{j,\text{exo}}}{2\sqrt{\pi}} \left(\frac{2k_B T_{\text{eff}}}{m_j} \right)^{0.5} (1 + \lambda_{\text{esc}}) \exp(-\lambda_{\text{esc}}) \tag{43}$$

The mean molar mass factor used to convert the loss rate from molecules s^{-1} to kg s^{-1} in both Jeans and Hydrodynamic escape was left constant (m_i), as m_j was assumed to be an infinitely dilute component of the atmosphere only (that is, $x_i \gg x_j$). Thus, the theoretical isotope fractionation was calculated for each element, presuming that they all had the same values of m_i and m_j.

Compositional evolution. The activity, a, of each element, i, in any planetary body is given by:

$$a_i = \frac{\left(\frac{(x_i \gamma_i)_{\text{planet}}}{(x_i \gamma_i)_{\text{initial}}} \right)}{\sum_i a_{i_{\text{planet}}}}, \tag{44}$$

where $(x_i \gamma_i)_{\text{initial}}$ is given for each i by a Gaussian distribution centred at 1,350 K, whose coefficients are adjusted such that the total pressure evolved as a function of temperature fits that for thermodynamic models for vaporization of a BSE composition[66] (Supplementary Fig. 2 and equation (20)). For simplicity, we assumed ideal solutions of each element, $\gamma_i = 1$. In the entire planet, therefore:

$$\sum_i a_i = \sum_i x_i = 1 \tag{45}$$

The composition and total pressure of the gas phase in equilibrium with the planet at each temperature step was calculated as detailed in 'Vapour pressure calculations', a proportion of which was lost by Jeans or hydrodynamic escape, for which a mass flux was determined (that is, a loss of mass over a time interval, see 'Atmospheric loss'). As the mass of the planet was known, this could be expressed in terms of the total planetary mass, which gave the normalized loss rate in seconds:

$$\frac{d\mathbf{m}}{dt} = \frac{\left(\frac{dm}{dt} \right)_{\text{loss}}}{M_{\text{planet}}} \tag{46}$$

In the model, the temperature was evaluated for a fixed time interval, dt, dictated by the time taken for the planet to cool by 10 K. Hence, multiplying the normalized loss rate by the seconds elapsed during the cooling interval gave the integrated mass loss (expressed as fraction of planetary mass) over that time interval:

$$d\mathbf{m} = \frac{d\mathbf{m}}{dt} dt \tag{47}$$

The new activity of a given element is:

$$a_{i+1} = a_i - d\mathbf{m} \frac{p_i}{P_T}, \tag{48}$$

Where $\frac{p_i}{P_T}$ is the mole fraction of the element i in the gas phase being lost. Here we assumed that there was no fractionation of elemental mole fractions in the gas at the loss surface with respect to that set by equilibrium with the magma ocean at the planetary surface. That is, we neglected processes in the stratosphere that may fractionate elements according to their scale heights because the molar mass of the atmosphere was assigned as a bulk property, not a sum across each fictive element.

The output composition was then normalized to the new total mass of the body; that is:

$$\mathbf{a}_{i+1} = \frac{a_{i+1}}{(\mathbf{m} - d\mathbf{m})} \tag{49}$$

This process was repeated in 10 K steps, and is manifested as a change in composition of the planet dictated by the element's volatility and the rate of atmospheric loss. Compositional evolution with time is shown in Supplementary Fig. 4. For isotope fractionation, this process was performed for elements i and j simultaneously throughout, such that the isotope composition (in ‰) of the body could be calculated at any time according to:

$$^{j/i}\delta_{\text{planet}} = \left(\frac{\mathbf{a}_j}{\mathbf{a}_i} - 1 \right) \times 1,000 \tag{50}$$

Monte Carlo simulations. For each simulation, there were three random variables:

(1) $\dot{M}$. It set the initial abundances of all planetesimals and embryos. $\dot{M}$ was randomly varied according to a normal distribution with a mean of $1 \times 10^{-7} M_\odot$ and a standard deviation (σ) of $0.25 \times 10^{-7} M_\odot$ in accordance with observations of T-Tauri stars[71]. These accretion rates yielded temperatures (at 0.7 au) of $1,380^{+145}_{-220}$ K (1σ), bracketing the T_c^{50} of the major rock-forming elements. This range of temperatures was employed because RLEs ($T_c^{50} \geq 1,400$ K) are unfractionated from one another in planetary materials[72], providing empirical evidence that there was no appreciable accretion of components with fractionated abundances of elements with $T_c^{50} \geq 1,400$ K.

(2) σ_{embryo}. It was randomly varied with a normal distribution with a mean of 87 K and $\sigma = 24$ K about the mean T_{midplane} value of the embryo in each simulation. This physically related to embryo accretion from planetesimals sourced from variably wide heliocentric feeding zones[25,73]. Low values of σ_{embryo} resulted in a step-function distribution of elements, similar to planetesimals, whereas high values of σ_{embryo} pertained to the accretion of planetesimals from a wider temperature range, leading to a smoother element distribution pattern in embryos as a function of T_c^{50}.

(3) m_i. A bulk property of the atmosphere, it was sampled randomly from a normal distribution with mean 33.5 g mol^{-1} and $\sigma = 3.5$ g/ mol^{-1}, with minima and maxima corresponding to the masses of Na(g) (23 g mol^{-1}) and SiO(g)/ CO$_2$(g) (both 44 g mol^{-1}), respectively. These were likely to represent the limits of the most abundant elements in a high-temperature vapour in equilibrium with a silicate mantle[66].

Monte Carlo simulations were performed with 1,000 iterations for each N-body simulation, in which the three variables were fixed for each simulation, selected according to the range and σ for each normal distribution. Sensitivity tests to determine how each parameter influenced the final elemental abundance of the Earth analogue are shown in Supplementary Fig. 5. The entire process described above was coded together in a Python script, and was run on the Ludwig-Maximilians-Universität supercomputing cluster. Each simulation took roughly 1 min to complete (1,000 simulations = 1,000 min).

Pebble accretion simulation. To simulate the accretion of the Earth predominantly by pebbles[74], a simple model was presented, in which the Earth grew to 90 % of its current mass solely by pebble accretion in 3.85 Myr. This process imparts heating due to the release of gravitational potential energy; from which a surface temperature was determined.

Because pebbles are small (~centimetre sized) they thermally equilibrate with the surrounding nebular gas at the locus of accretion, that is, at 1 au for the Earth. To calculate the temperature at 1 au, an estimation of how the mass accretion rate to the Sun decays as a function of time was required. To do so, equation (4) of ref. [21], based on observations of the mass accretion rates of T-Tauri stars, was used to calculate $\dot{M}$ (equation (3)). For each given time step (t), the corresponding value of $\dot{M}$ was inserted into equation (2) to calculate the temperature of the accreting pebbles. Pebble fluxes were assumed to mirror mass accretion rates (equation (3)) and scale with $M_E^{2/3}$, typical of two-dimensional pebble accretion in the Hill regime[47]. For a given temperature, their composition was determined in a manner analogous to that for planetesimals (see 'Disk structure and initial composition' above). The first and second terms of equation (3) were varied within their uncertainties in a Monte Carlo simulation to evaluate the sensitivity of the Earth's composition to the mass accretion rate.

Because equation (2) predicted very high temperatures in the first few thousand years (up to 3,800 K at 5,000 yr), a saturation limit was placed at 1,350 K, which affected only the first 1.5 ± 0.5% of material accreted to the Earth. The vapour pressures, atmospheric loss and compositional evolution of Earth were treated in an identical manner to that outlined above, determined by the surface temperature given in the pebble accretion simulation.

Data availability

Raw data produced by the numerical models are provided via Zenodo at https://doi.org/10.5281/zenodo.6412661. Interested parties may contact S.A.J. and A.M. to access the output of N-body and pebble accretion simulations upon reasonable request. All other data supporting the findings of this study are available within the paper and its Supplementary Information.

Code availability

References

1. Wetherill, G. W. Formation of the Earth. *Annu. Rev. Earth Planet. Sci.* **18**, 205–256 (1990).
2. Wetherill, G. W. Provenance of the terrestrial planets. *Geochim. Cosmochim. Acta* **58**, 4513–4520 (1994).
3. Chambers, J. E. Making more terrestrial planets. *Icarus* **152**, 205–224 (2001).
4. Drążkowska, J. & Alibert, Y. Planetesimal formation starts at the snow line. *Astron. Astrophys.* **608**, A92 (2017).
5. Johansen, A. et al. A pebble accretion model for the formation of the terrestrial planets in the Solar System. *Sci. Adv.* **7**, eabc0444 (2021).
6. Palme, H. & O'Neill, H. S. C. in *Treatise on Geochemistry* Vol. 3 (ed Carlson, R. W.) 1–39 (Elsevier, 2014).
7. Sossi, P. A., Nebel, O., O'Neill, H. S. C. & Moynier, F. Zinc isotope composition of the Earth and its behaviour during planetary accretion. *Chem. Geol.* **477**, 73–84 (2018).
8. Wang, K. & Jacobsen, S. B. Potassium isotopic evidence for the origin of the Moon. *Nature* **538**, 487–490 (2016).
9. Sharp, Z. D. et al. The chlorine isotope composition of chondrites and Earth. *Geochim. Cosmochim. Acta* **107**, 189–204 (2013).
10. Pringle, E. A. & Moynier, F. Rubidium isotopic composition of the Earth, meteorites, and the Moon: evidence for the origin of volatile loss during planetary accretion. *Earth Planet. Sci. Lett.* **473**, 62–70 (2017).
11. Humayun, M. & Clayton, R. N. Potassium isotope cosmochemistry: genetic implications of volatile element depletion. *Geochim. Cosmochim. Acta* **59**, 2131–2148 (1995).
12. Albarède, F. Volatile accretion history of the terrestrial planets and dynamic implications. *Nature* **461**, 1227–1233 (2009).
13. Larimer, J. W. Chemical fractionations in meteorites–I. Condensation of the elements. *Geochim. Cosmochim. Acta* **31**, 1215–1238 (1967).
14. Sossi, P. A., Klemme, S., O'Neill, H. S. C., Berndt, J. & Moynier, F. Evaporation of moderately volatile elements from silicate melts: experiments and theory. *Geochim. Cosmochim. Acta* **260**, 204–231 (2019).
15. Campbell, I. H. & O'Neill, H. S. C. Evidence against a chondritic Earth. *Nature* **483**, 553–558 (2012).
16. Braukmüller, N., Wombacher, F., Funk, C. & Münker, C. Earth's volatile element depletion pattern inherited from a carbonaceous chondrite-like source. *Nat. Geosci.* **12**, 564–569 (2019).
17. Jacobson, S. A. & Morbidelli, A. Lunar and terrestrial planet formation in the Grand Tack scenario. *Phil. Trans. R. Soc. A* **372**, 20130174 (2014).
18. Rubie, D. C. et al. Accretion and differentiation of the terrestrial planets with implications for the compositions of early-formed Solar System bodies and accretion of water. *Icarus* **248**, 89–108 (2015).
19. Bell, K. R., Cassen, P. M., Klahr, H. H. & Henning, T. The structure and appearance of protostellar accretion disks: limits on disk flaring. *Astron. J.* **486**, 372–387 (1997).
20. Dullemond, C. P. & Monnier, J. D. The inner regions of protoplanetary disks. *Annu. Rev. Astron. Astrophys.* **48**, 205–239 (2010).
21. Bitsch, B., Johansen, A., Lambrechts, M. & Morbidelli, A. The structure of protoplanetary discs around evolving young stars. *Astron. Astrophys.* **575**, A28 (2015).
22. Lodders, K. Solar system abundances and condensation temperatures of the elements. *Astrophys. J.* **591**, 1220–1247 (2003).
23. Wood, B. J., Smythe, D. J. & Harrison, T. The condensation temperatures of the elements: a reappraisal. *Am. Mineral.* **104**, 844–856 (2019).
24. Jeans, J. H. *The Dynamical Theory of Gases* (Univ. Cambridge, 1925).
25. Fischer, R. A. & Ciesla, F. J. Dynamics of the terrestrial planets from a large number of N-body simulations. *Earth Planet. Sci. Lett.* **392**, 28–38 (2014).
26. Pierrehumbert, R. T. *Principles of Planetary Climate* (Cambridge Univ. Press, 2010).
27. Genda, H. & Abe, Y. Enhanced atmospheric loss on protoplanets at the giant impact phase in the presence of oceans. *Nature* **433**, 842–844 (2005).
28. Schönbächler, M., Carlson, R. W., Horan, M. F., Mock, T. D. & Hauri, E. H. Heterogeneous accretion and the moderately volatile element budget of Earth. *Science* **328**, 884–887 (2010).
29. Mezger, K., Maltese, A. & Vollstaedt, H. Accretion and differentiation of early planetary bodies as recorded in the composition of the silicate Earth. *Icarus* **365**, 114497 (2021).
30. Norris, C. A. & Wood, B. J. Earth's volatile contents established by melting and vaporization. *Nature* **549**, 507–510 (2017).
31. Woolum, D. S. & Cassen, P. Astronomical constraints on nebular temperatures: implications for planetesimal formation. *Meteorit. Planet. Sci.* **34**, 897–907 (1999).
32. Morbidelli, A. et al. Contemporary formation of early Solar System planetesimals at two distinct radial locations. *Nat. Astron.* **6**, 72–79 (2022).
33. Lichtenberg, T., Drazkowska, J., Schönbächler, M., Golabek, G. J. & Hands, T. O. Bifurcation of planetary building blocks during Solar System formation. *Science* **371**, 365–370 (2021).
34. Hans, U., Kleine, T. & Bourdon, B. Rb–Sr chronology of volatile depletion in differentiated protoplanets: BABI, ADOR and ALL revisited. *Earth Planet. Sci. Lett.* **374**, 204–214 (2013).
35. Anand, A., Pape, J., Wille, M., Mezger, K. & Hofmann, B. Early differentiation of magmatic iron meteorite parent bodies from Mn-Cr chronometry. *Geochem. Perspect. Lett.* **20**, 6–10 (2021).
36. Trinquier, A., Birck, J.-L., Allègre, C. J., Göpel, C. & Ulfbeck, D. ^{53}Mn–^{53}Cr systematics of the early Solar System revisited. *Geochim. Cosmochim. Acta* **72**, 5146–5163 (2008).
37. Dauphas, N., Poitrasson, F., Burkhardt, C. & Kobayashi, H. Planetary and meteoritic Mg/Si and δ^{30}Si variations inherited from solar nebula chemistry. *Earth Planet. Sci. Lett.* **427**, 236–248 (2015).
38. Sossi, P. A., Nebel, O., Anand, M. & Poitrasson, F. On the iron isotope composition of Mars and volatile depletion in the terrestrial planets. *Earth Planet. Sci. Lett.* **449**, 360–371 (2016).
39. Hin, R. C. et al. Magnesium isotope evidence that accretional vapour loss shapes planetary compositions. *Nature* **549**, 511–515 (2017).
40. Young, E. D. et al. Near-equilibrium isotope fractionation during planetesimal evaporation. *Icarus* **323**, 1–15 (2019).
41. Tian, Z. et al. Potassium isotopic compositions of howardite-eucrite-diogenite meteorites. *Geochim. Cosmochim. Acta* **266**, 611–632 (2019).
42. Paniello, R. C., Day, J. M. D. & Moynier, F. Zinc isotopic evidence for the origin of the Moon. *Nature* **490**, 376–379 (2012).
43. Stephant, A. et al. The chlorine isotopic composition of the Moon: insights from melt inclusions. *Earth Planet. Sci. Lett.* **523**, 115715 (2019).
44. Grimm, R. E. & McSween, H. Y. Heliocentric zoning of the asteroid belt by aluminum-26 heating. *Science* **259**, 653–656 (1993).
45. Moskovitz, N. & Gaidos, E. Differentiation of planetesimals and the thermal consequences of melt migration. *Meteorit. Planet. Sci.* **46**, 903–918 (2011).
46. Schiller, M., Bizzarro, M. & Siebert, J. Iron isotope evidence for very rapid accretion and differentiation of the proto-Earth. *Sci. Adv.* **6**, eaay7604 (2020).
47. Lambrechts, M. & Johansen, A. Rapid growth of gas-giant cores by pebble accretion. *Astron. Astrophys.* **544**, A32 (2012).
48. Kurokawa, H. & Tanigawa, T. Suppression of atmospheric recycling of planets embedded in a protoplanetary disc by buoyancy barrierc. *Mon. Not. R. Astron. Soc.* **479**, 635–648 (2018).
49. Tian, Z. et al. Potassium isotope composition of Mars reveals a mechanism of planetary volatile retention. *Proc. Natl Acad. Sci. USA* **118**, e2101155118 (2021).
50. Humayun, M. & Cassen, P. in *The Origin of the Earth and Moon* (eds Canup, R. M. & Righter, K.) 3–23 (Univ. Arizona Press, 2000).
51. Charnoz, S. et al. Planetesimal formation in an evolving protoplanetary disk with a dead zone. *Astron. Astrophys.* **627**, A50 (2019).
52. Beckwith, S. V. W. & Sargent, A. I. Molecular line emission from circumstellar disks. *Astrophys. J.* **402**, 280–291 (1993).
53. Ahrens, T. J. & O'Keefe, J. D. Shock melting and vaporization of lunar rocks and minerals. *Moon* **4**, 214–249 (1972).
54. Pierazzo, E. & Melosh, H. J. Understanding oblique impacts from experiments, observations, and modeling. *Annu. Rev. Earth Planet. Sci.* **28**, 141–167 (2000).
55. Melosh, H. J. in *Origin of the Earth* (eds Newsom, H. E. & Jones, J. H.) 69–83 (Oxford Univ., 1990).
56. Lesher, C. E. & Spera, F. J. in *The Encyclopedia of Volcanoes* 113–141 (Elsevier Inc., 2015).
57. Bouhifd, M. A. et al. Thermochemistry and melting properties of basalt. *Contrib. Mineral. Petrol.* **153**, 689–698 (2007).
58. Connolly, J. A. D. Liquid-vapor phase relations in the Si-O system: A calorically constrained van der Waals-type model. *J. Geophys. Res. Planets* **121**, 1641–1666 (2016).
59. Xiao, B. & Stixrude, L. Critical vaporization of MgSiO$_3$. *Proc. Natl Acad. Sci. USA* **115**, 5371–5376 (2018).
60. Nakajima, M. & Stevenson, D. J. Melting and mixing states of the Earth's mantle after the Moon-forming impact. *Earth Planet. Sci. Lett.* **427**, 286–295 (2015).
61. Bower, D. J. et al. Linking the evolution of terrestrial interiors and an early outgassed atmosphere to astrophysical observations. *Astron. Astrophys.* **631**, A103 (2019).
62. Nikolaou, A. et al. What factors affect the duration and outgassing of the terrestrial magma ocean? *Astrophys. J.* **875**, 11 (2019).
63. Lebrun, T. et al. Thermal evolution of an early magma ocean in interaction with the atmosphere. *J. Geophys. Res. Planets* **118**, 1155–1176 (2013).

64. Sossi, P. A. & Fegley, B. Thermodynamics of element volatility and its application to planetary processes. *Rev. Mineral. Geochem.* **84**, 393–459 (2018).

65. Grossman, L., Beckett, J. R., Fedkin, A. V., Simon, S. B. & Ciesla, F. J. Redox conditions in the solar nebula: observational, experimental, and theoretical constraints. *Rev. Mineral. Geochem.* **68**, 93–140 (2008).

66. Visscher, C. & Fegley, B. Chemistry of impact-generated silicate melt-vapor debris disks. *Astrophys. J.* **767**, L12 (2013).

67. Solomatov, V. in *Treatise on Geophysics* 2nd edn (ed Schubert, G.) Vol. 9, 81–104 (Elsevier B.V., 2015).

68. Corgne, A., Liebske, C., Wood, B. J., Rubie, D. C. & Frost, D. J. Silicate perovskite-melt partitioning of trace elements and geochemical signature of a deep perovskitic reservoir. *Geochim. Cosmochim. Acta* **69**, 485–496 (2005).

69. Hunten, D. M. The escape of light gases from planetary atmospheres. *J. Atmos. Sci.* **30**, 1481–1494 (1973).

70. Charnoz, S. et al. Tidal pull of the Earth strips the proto-Moon of its volatiles. *Icarus* **364**, 114451 (2021).

71. Gullbring, E., Hartmann, L., Briceño, C. & Calvet, N. Disk accretion rates for T Tauri stars. *Astron. J.* **492**, 323–341 (1998).

72. O'Neill, H. S. C. & Palme, H. Collisional erosion and the non-chondritic composition of the terrestrial planets. *Phil. Trans. R. Soc. A* **366**, 4205–4238 (2008).

73. Kaib, N. A. & Cowan, N. B. The feeding zones of terrestrial planets and insights into Moon formation. *Icarus* **252**, 161–174 (2015).

74. Johansen, A. & Lambrechts, M. Forming planets via pebble accretion. *Annu. Rev. Earth Planet. Sci.* **45**, 359–387 (2017).

75. Mittlefehldt, D. W. Asteroid (4) Vesta: I. The howardite-eucrite-diogenite (HED) clan of meteorites. *Chem. Erde* **75**, 155–183 (2015).

76. Fegley, B. & Schaefer, L. in *Principles and Perspectives in Cosmochemistry* (eds Goswami, A. & Reddy, B. E.) 347–377 (Springer, 2010).

77. Siebert, J. et al. Chondritic Mn/Na ratio and limited post-nebular volatile loss of the Earth. *Earth Planet. Sci. Lett.* **485**, 130–139 (2018).

78. Wanke, H. & Dreibus, G. Chemical composition and accretion history of terrestrial planets. *Phil. Trans. R. Soc. A* **325**, 545–557 (1988).

Author contributions

P.A.S. conceived the study, developed the governing equations and assisted with writing the Python code. I.L.S. developed the Python code and ran simulations. S.A.J. performed the *N*-body simulations. A.M. performed the *N*-body and pebble accretion simulations. H.S.C.O. contributed to the conceptual development of the study. P.A.S. wrote the paper with input from A.M. and H.S.C.O. All authors contributed to the discussion of the results.

Competing interests

The authors declare no competing interests.

Additional information

Extended data is available for this paper at https://doi.org/10.1038/s41550-022-01702-2.

Supplementary information The online version contains supplementary material available at https://doi.org/10.1038/s41550-022-01702-2.

Correspondence and requests for materials should be addressed to Paolo A. Sossi.

Peer review information *Nature Astronomy* thanks Matt Clement and the other, anonymous, reviewer(s) for their contribution to the peer review of this work.

Reprints and permissions information is available at www.nature.com/reprints.

Publisher's note Springer Nature remains neutral with regard to jurisdictional claims in published maps and institutional affiliations.
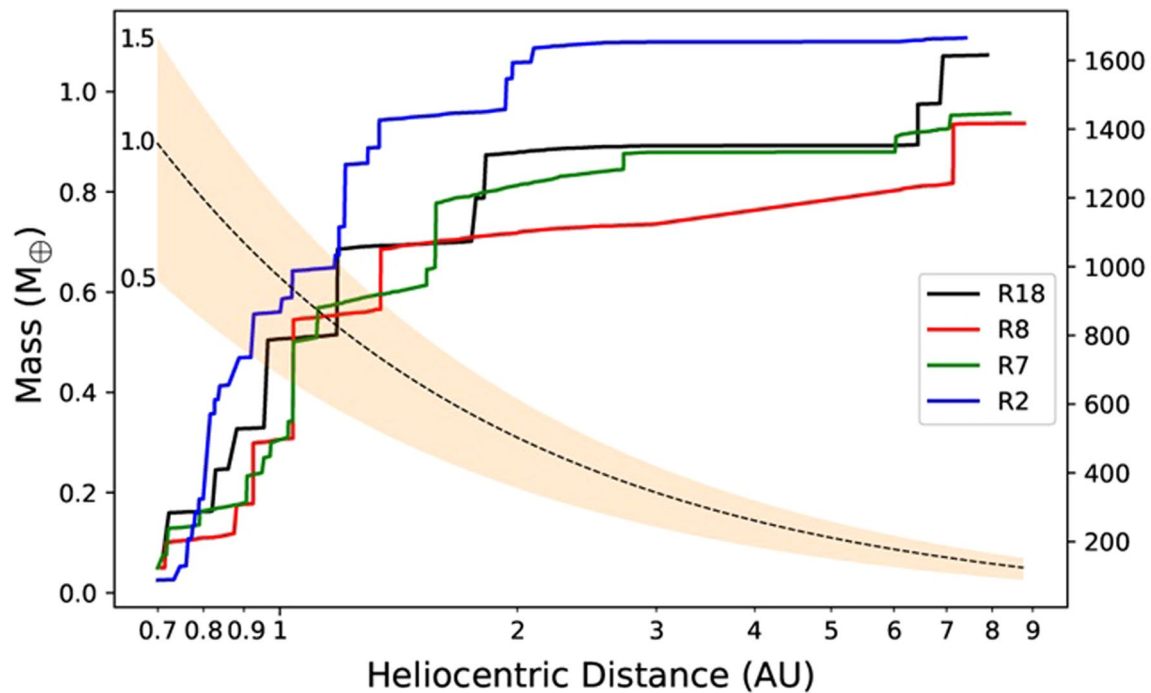
**Extended Data Fig. 1 | The cumulative radial distribution (in AU) of the mass (in Earth masses, M$_E$) of accreted components to the Earth analogue planet.** The lines indicate the mass accreted up to a given heliocentric distance, while the colours represent the different Grand Tack *N*-body simulations (black = R18, red = R8, green = R7, blue = R2). The heliocentric distances (AU) up to which material is sourced for 10%, 50% and 90% of the planet growth are, respectively, R18–0.72, 1.18, 6.43; R8–0.76, 1.04, 7.13; R7–0.72, 1.04, 2.73; R2–0.77, 0.93, 1.93. The secondary y-axis shows the midplane temperature ($T_{midplane}$) in K calculated with Eq. 1 for three mass accretion rates, 1.5, 1.0 and 0.5 × 10^{-7} solar masses/yr depicted, respectively, as the upper brown envelope, dashed curve and lower brown envelope.
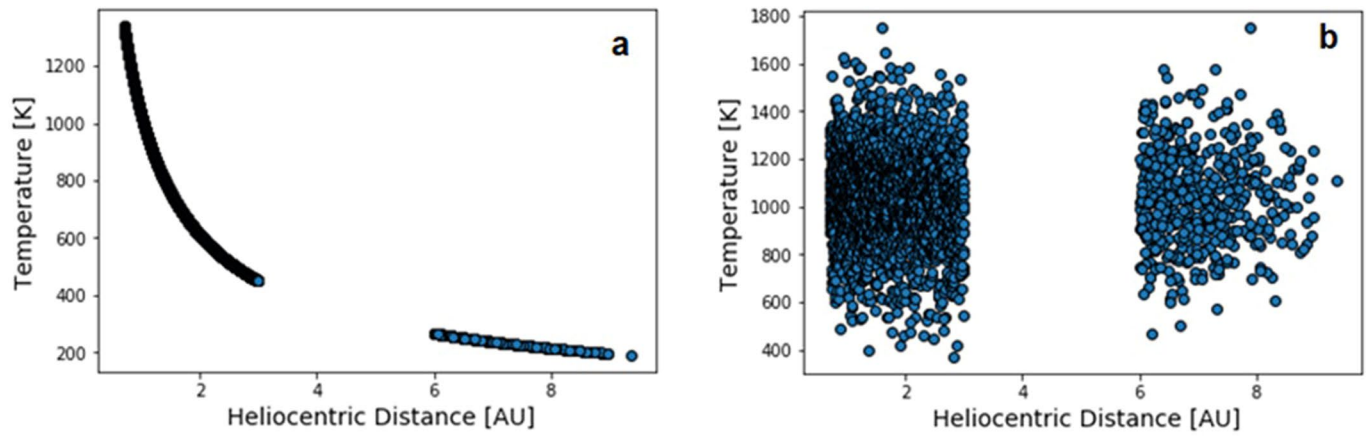
Extended Data Fig. 2 | Initial temperature distributions among planetesimals and embryos in N-body simulation GT/8:1/0.025/R2. a, Initial temperatures imposed by Eq. (2), according to $\dot{M} = 1 \times 10^{-7}$ solar masses/yr. **b**, The alternative hypothesis, in which initial temperatures are randomly selected from a normal distribution that is intended to simulate ^{26}Al heating independent of heliocentric distance, here 1000 ± 175 K.
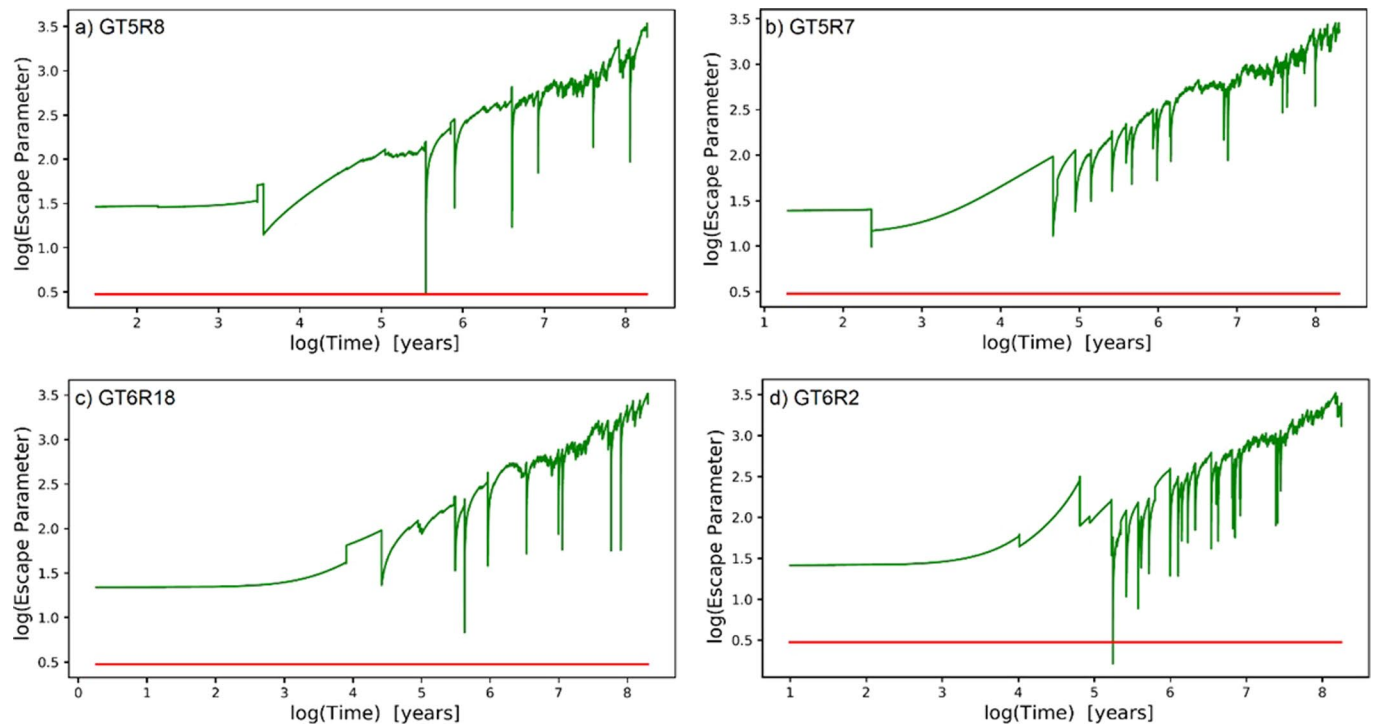
Extended Data Fig. 3 | The tendency for atmospheric loss to occur from the proto-Earth analogue as a function of its accretion time for four *N*-body simulations. Examples of the evolution of the log(escape parameter) for the growing Earth analogue in each of the four N-body simulations, in which the escape parameter is calculated with $m_i = 33.5$ g/mol (the mean value of the Monte Carlo simulations). The red horizontal line denotes the threshold value at which Jeans (above) and Hydrodynamic escape (below) prevail. Negative spikes record impact events leading to temperature increases, superimposed upon the longer-wavelength trend of increasing λ_{esc} as accretion proceeds and the proto-Earth analogue grows to its final mass. This attests to the increasing difficulty of atmospheric loss to occur during progressively later stages of accretion, a result consistent among all N-body simulations. Simulation 'GT6R2' represents the most energetic accretion pathway for the Earth analogue, while simulation 'GT5R7' is the most tranquil.
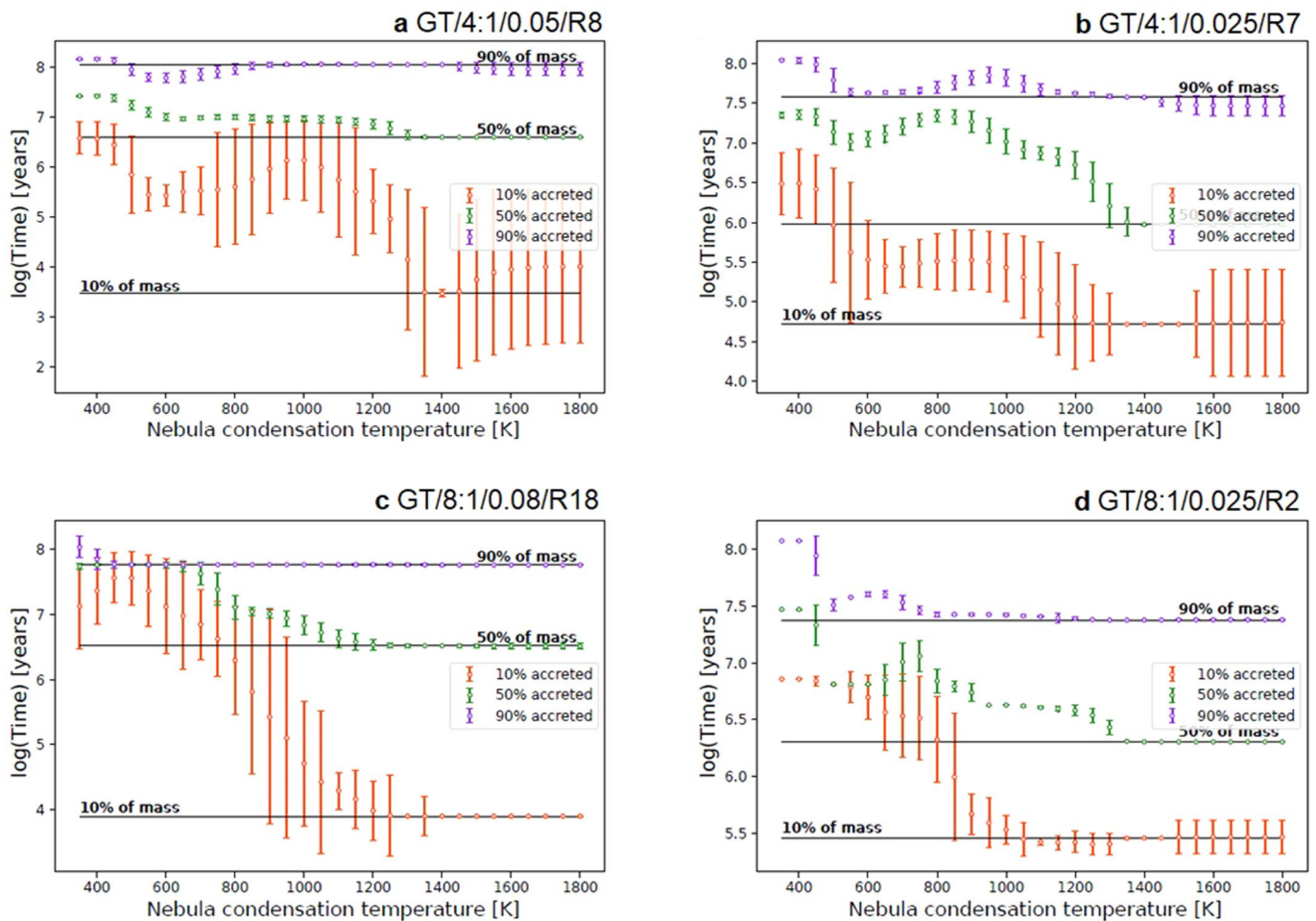
Extended Data Fig. 4 | Timing of element accretion to the Earth analogue as a function of volatility for four N-body simulations. Points represent the time in the N-body simulation (ordinate) at which a given element (abscissa) reaches a threshold value, y, (10 %, red; 50 %, green; or 90 %, purple) of its final abundance in the Earth analogue. These points are y_i % accreted $= 100 \times (x_i M)_t / (x_i M)_f$, where the subscripts t and f denote the threshold time and the final time, respectively, x is the element mole fraction and M the mass of the body. Error bars (1 standard deviation, 1σ) denote the range given by Monte Carlo models for different $\dot{M}$, σ_{embryo} and m_i across 1000 simulations. No error bar indicates that the element reaches the given % accreted value at the same time in each MC simulation. The mass of the Earth, M_t / M_f, is denoted by horizontal lines at 10 %, 50 % and 90 %. The offsets between these lines and the coloured points indicate differential accretion times. The scatter in the refractory element accretion times reflects their enrichment/dilution by the absence/presence of more abundant elements with T_c^{50} around 1350 K, as indicated by their consistent accretion times.
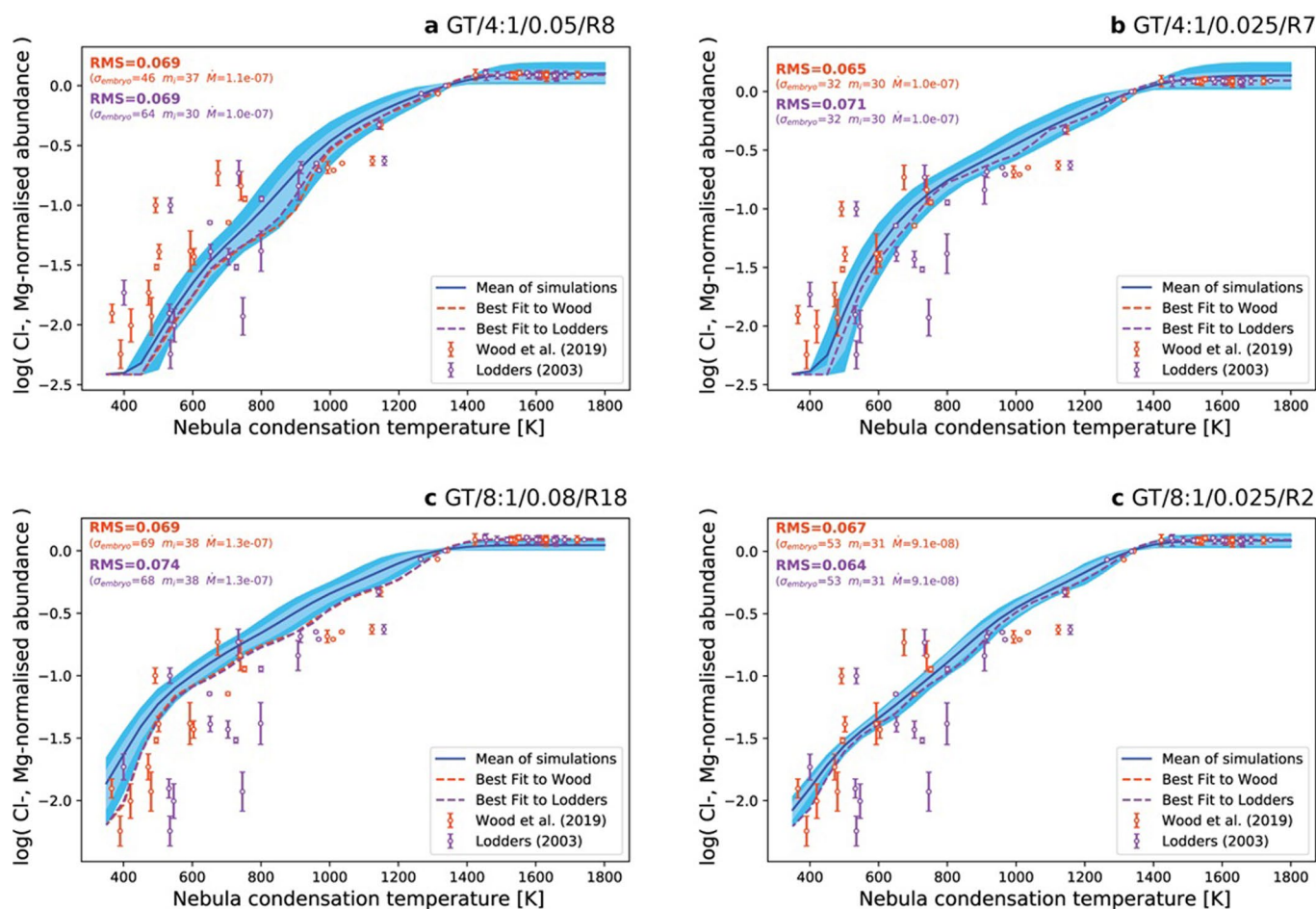
Extended Data Fig. 5 | Elemental abundances in the fully accreted Earth for four N-body simulations. CI-, Mg-normalised elemental abundances in the BSE[6] as a function of 50% nebular condensation temperatures (red[23]; purple[22,76]), compared with abundances predicted by 1000 Monte Carlo simulations per N-body simulation. The average composition of the Earth analogue over 1000 runs is given by the solid blue line, with its percentile range (25th to 75th, light blue and 10th to 90th, dark blue). The dashed black line shows the single simulation that minimises the Root-Mean-Square (RMS) deviation from the data. The RMS values are listed in the top left-hand corner, along with the values of the three random variables to which they correspond. Only lithophile elements were plotted as siderophile elements are further depleted by core formation, which is not considered in our model.
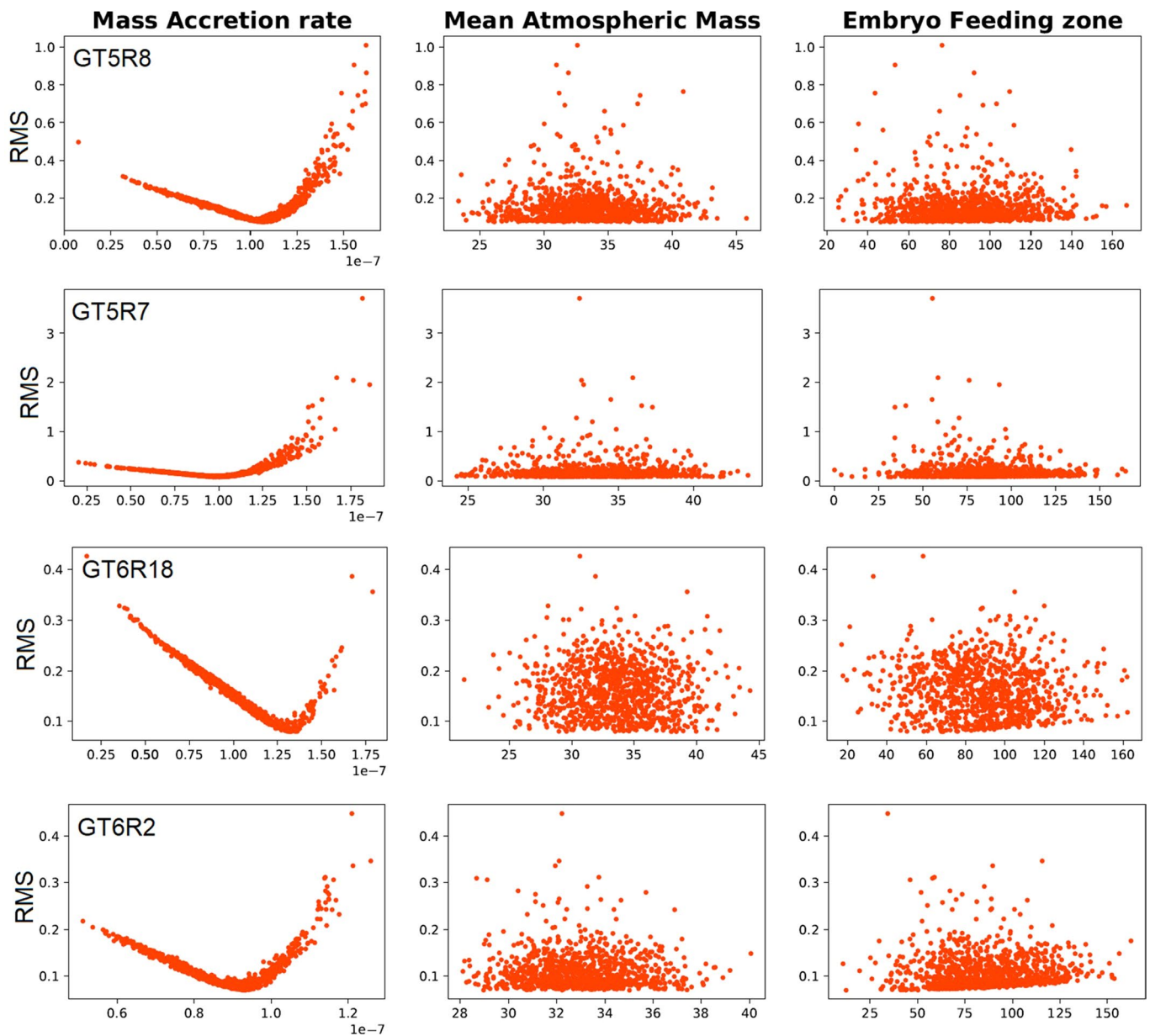
Extended Data Fig. 6 | Variation of the Root-Mean-Square Deviation (RMS) to the observed elemental abundances as a function of the three randomised variables in 1000 Monte Carlo simulations. The four N-body simulations are organised by row, in which the RMS is plotted on the ordinate axis and the value of the random variable on the abscissa, organised by column (mass accretion rate ($\dot{M}$), mean atmospheric mass (m_i) and embryo feeding zone (σ_{embryo}). Although the goodness of fit is nearly independent of σ_{embryo} and m_i, it has a well-defined minimum as a function of mass accretion rate. The mass accretion rate defined by this minimum varies only marginally among the four N-body simulations, with a mean of $1.08(\pm0.17)\times10^{-7}$ solar masses/year, demonstrating that the composition of the fully accreted Earth analogue is largely sensitive to the initial compositions of its constituents, which are in turn set by the temperatures (and hence heliocentric distances) at which they were formed.
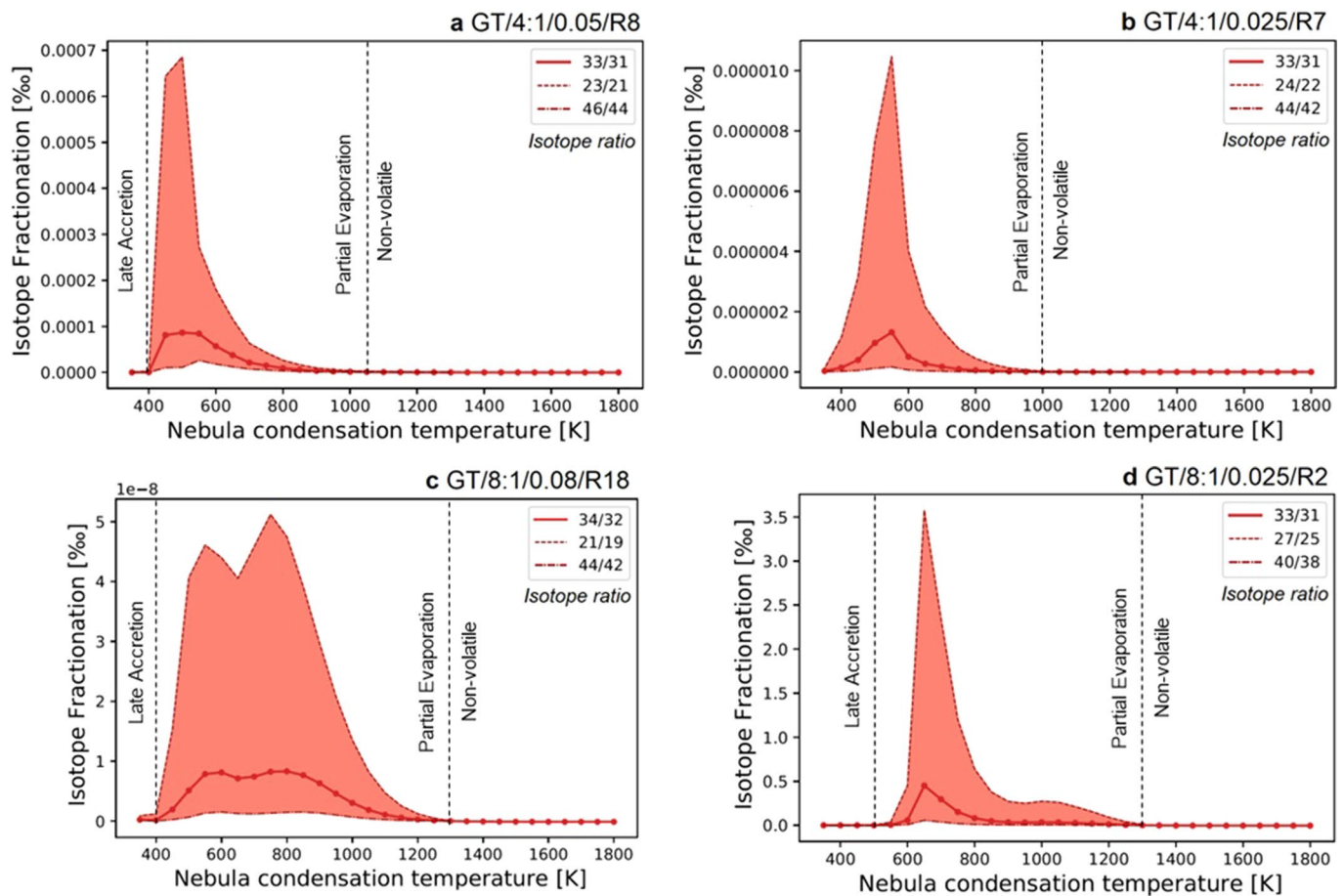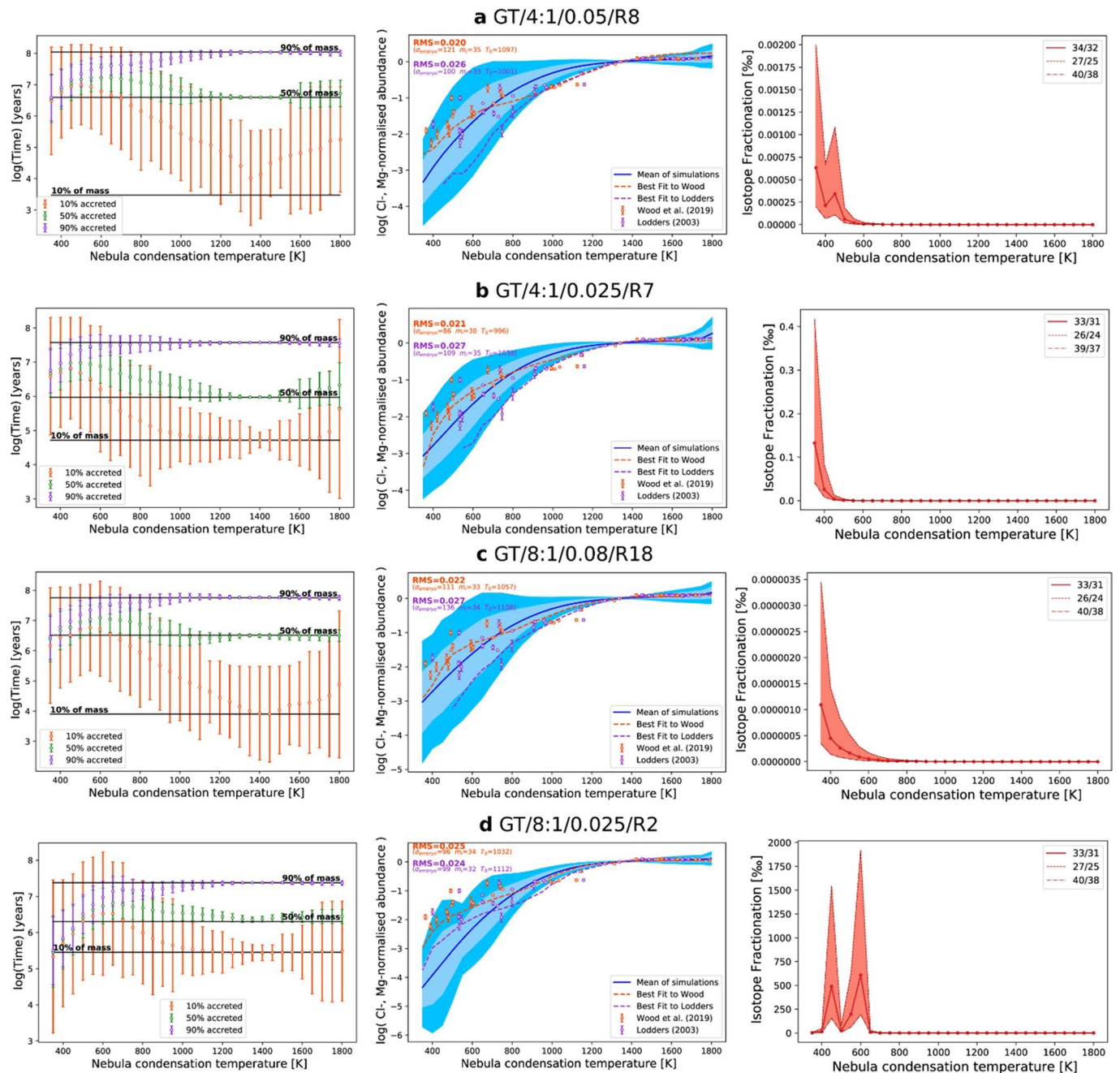
Extended Data Fig. 7 | Stable isotope fractionation for each fictive element in the fully accreted Earth analogue as a function of volatility for four N-body simulations. The red line indicates the mean isotopic fractionation (in per mille relative to the initial value, that is, CI chondritic) in the fully accreted Earth analogue across 1000 Monte Carlo runs for each N-body simulation. The isotope ratio in g/mol (m_i = numerator isotope, Δm_i = 2 atomic mass units, amu) is listed in the legend. The vertical dashed lines delimit zones pertaining to Late Accretion (defined here as volatile elements whose isotopes are present in chondritic ratios), Partial Evaporation (elements bear an isotopic signature of partial evaporation during atmospheric loss) and Non-Volatile (elements were not lost and are also chondritic).

A) N-body simulation GT5R8
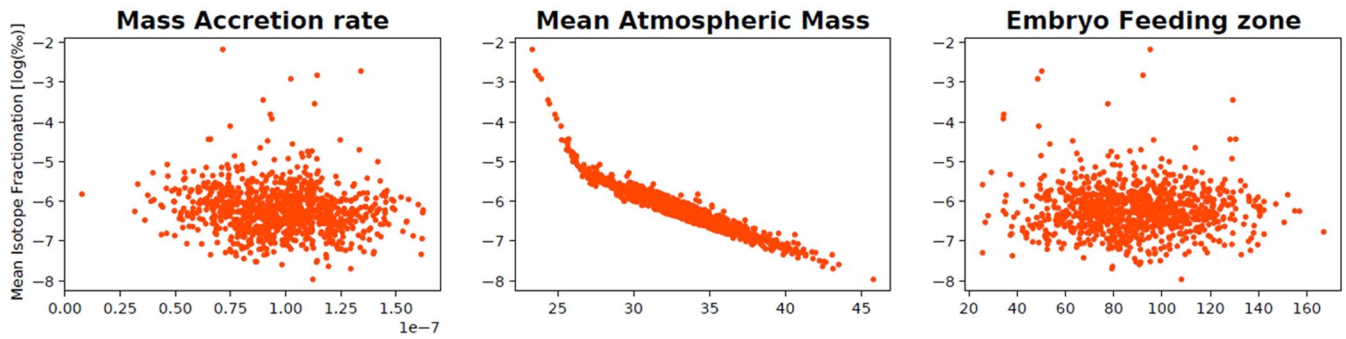
B) N-body simulation GT5R7
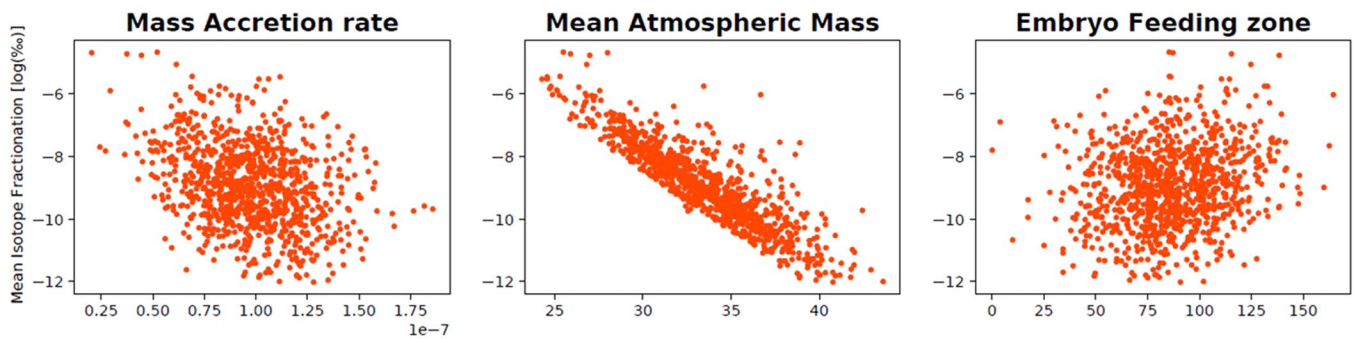
C) N-body simulation GT6R18
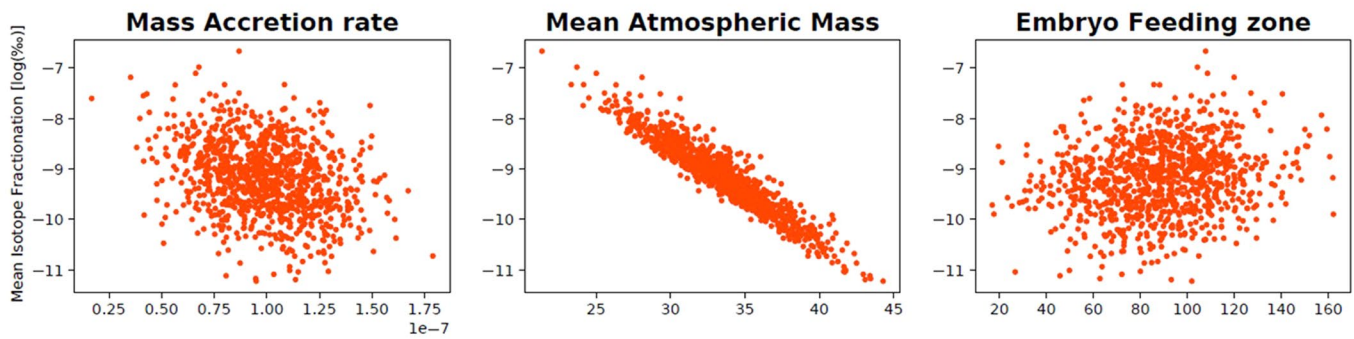
D) N-body simulation GT6R2
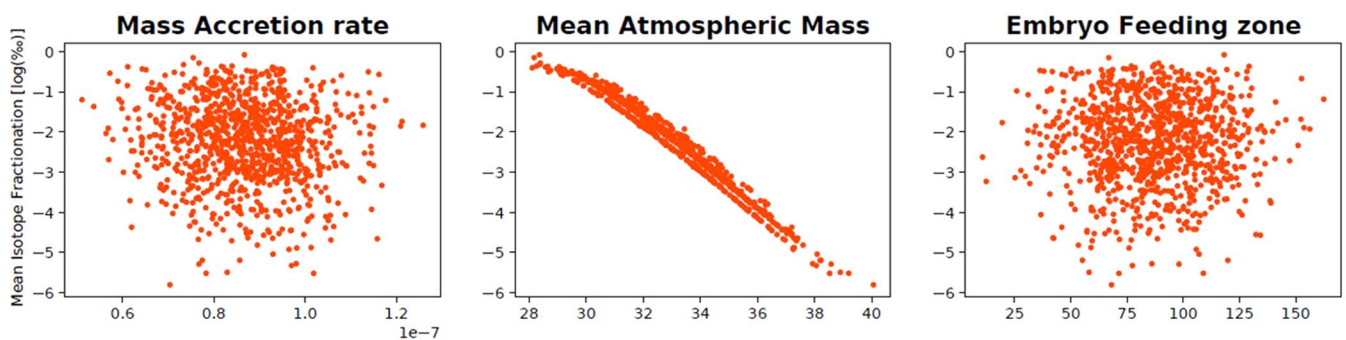
Extended Data Fig. 8 | See next page for caption.

Extended Data Fig. 8 | Variation of the average stable isotopic fractionation (expressed in log ‰) across all elements as a function of the three randomised variables in 1000 Monte Carlo simulations. The four N-body simulations are organised by row, in which the logarithm of the mean isotope fractionation is plotted on the ordinate axis and the value of the random variable on the abscissa, organised by column; mass accretion rate ($\dot{M}$) (in solar masses/yr), mean atmospheric mass (m_i) (in g/mol) and embryo feeding zone (σ_{embryo}) (in K). The degree of isotopic fractionation in the fully accreted Earth analogue is only mildly dependent on $\dot{M}$ and σ_{embryo}, but shows a strong negative correlation with the mean atmospheric mass, m_i, reflecting the scaling between atmospheric loss rate and atmosphere scale height with its molar mass. Changes in slope reflect the participation of different, major atmospheric loss events (hydrodynamic escape) engendered by multiple collisions.

Extended Data Fig. 9 | Composite plots of four N-body simulations for accretion time, bulk composition and isotope fractionation. From left to right, the panels are equivalent to Extended Data Figs. 4, 5 & 7, respectively. The results show that there is no systematic difference in the accretion times of the volatile- and non-volatile elements in the simulations (left-hand side panel). The middle panel illustrates that the bulk composition of the Earth can be reproduced using the initial conditions shown in Extended Data Fig. 2b. Isotopic fractionation (right-hand side panel) is always larger than for the equivalent simulation using the initial conditions shown in Extended Data Fig. 2a (compare with Extended Data Fig. 7). Due to the presence of volatile elements in the proto-Earth throughout its growth, most isotopic fractionation is seen in the most volatile elements, and the bimodal nature of the peaks (for example simulation GT/8:1/0.025/R2) carries the imprint of two separate collisional events.
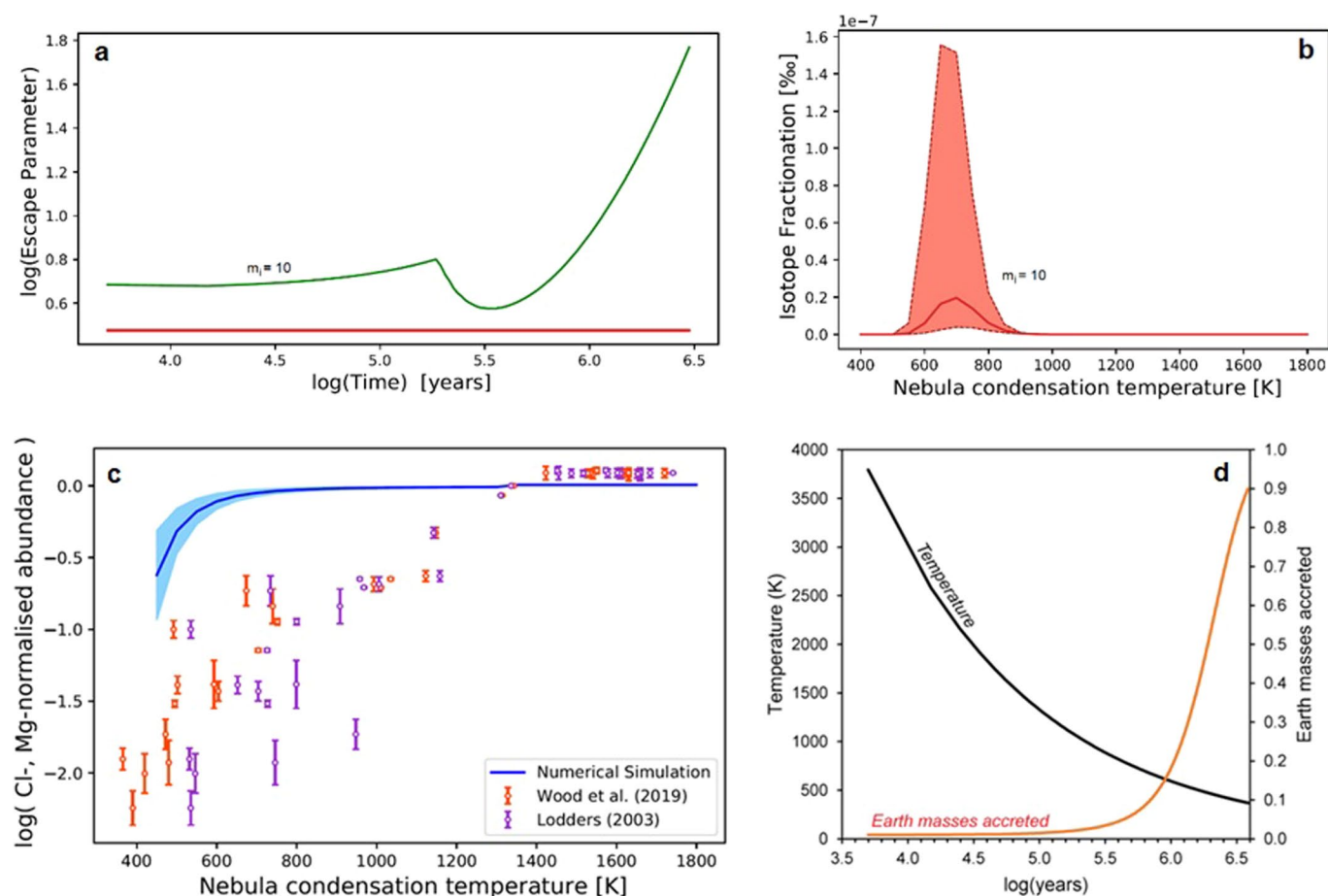
Extended Data Fig. 10 | Escape parameter, isotope composition, elemental abundances and accretion rate of the Earth in a pebble accretion scenario.
a, The escape parameter as a function of accretion time for a fixed mean atmospheric mass of 10 g/mol. Despite the lower mass, the proto-Earth never reaches a regime of hydrodynamic escape, due to the lower peak temperatures for a given mass with respect to planetesimal accretion. Because pebble accretion is continuous in time, the evolution of the escape parameter is devoid of any negative spikes. **b,** Consequently, evaporation and atmospheric loss is less marked than in the planetesimal accretion models, as attested to by the lesser degree of isotopic fractionation ($<2\times10^{-7}$ ‰) evolved in the Earth. The thick red line represents the mean value, with the red field corresponding to the maximum and minimum isotope fractionation experienced, as a function of nebular condensation temperature. As for the planetesimal accretion simulations, isotope fractionation is most marked for elements with T_c^{50} around ~700 K, representing those that are sufficiently volatile to record atmospheric loss, but not so volatile so as to have been overprinted by late-accreting material. **c,** The CI-, Mg-normalised elemental abundances in the BSE[6] relative to nebular condensation temperatures (red[23]; purple[22]) compared with abundances predicted from the pebble accretion simulation. The dark blue curve represents the mean and the blue field its $1s$ uncertainty propagated from Eq. (2). Accretion of pebbles also results in a smooth, concave-down pattern as a function of time. However, volatile element depletion for pebble accretion is less marked than in the planetesimal accretion model, reflecting a lower mean temperature of the accreting pebbles. If the pebble flux is increased and truncated when the Earth reaches its final mass (*for example*, by the formation of a Jupiter barrier) the Earth would accrete faster in a warmer disk, causing more depletion in elements with higher T_c^{50}. Nevertheless, the transition from undepleted to depleted elements would remain too abrupt in T_c^{50} relative to observations. **d,** The accretion rate of Earth (red curve) as a function of time, superimposed on the temperature evolution of the surrounding nebular gas at 1 AU (black curve), valid for accretion rates that scale with $M^{2/3}$. It shows that the temperature decrease occurs over too short a time interval, declining to ~500 K after ~10^6 yr, by which point the Earth has accreted only ~15 % of its total mass, meaning minimal volatile depletion is expressed in its final composition.